Ewiak, O., Victor, P., Oncken, O. (2015): Investigating multiple fault rupture at the Salar del Carmen segment of the Atacama Fault System (northern Chile): Fault scarp morphology and knickpoint analysissegment of the Atacama Fault System, northern Chile. - *Tectonics*, *34*, 2, p. 187-212.

DOI: http://doi.org/10.1002/2014TC003599

AGU PUBLICATIONS

Tectonics

RESEARCH ARTICLE
10.1002/2014TC003599

Key Points:
- Test the applicability of geomorphic markers to quantify paleoearthquakes
- Quantification of along-strike displacement from geomorphology
- Improvement of estimation of paleomagnitudes for multiple rupture fault scarps

Supporting Information:
- Readme
- Text S1
- Figure S1
- Figure S2
- Figure S3
- Figure S4
- Figure S5
- Figure S6
- Figure S7
- Figure S8
- Figure S9
- Figure S10

Correspondence to:
O. Ewiak,
oewiak@gfz-potsdam.de

Citation:
Ewiak, O., P. Victor, and O. Oncken (2015), Investigating multiple fault rupture at the Salar del Carmen segment of the Atacama Fault System (northern Chile): Fault scarp morphology and knickpoint analysis, *Tectonics, 34*, 187–212, doi:10.1002/2014TC003599.

Received 31 MAR 2014
Accepted 18 DEC 2014
Accepted article online 23 DEC 2014
Published online 3 FEB 2015
Corrected 13 MAR 2015

This article was corrected on 13 MAR 2015. See the end of the full text for details.

Investigating multiple fault rupture at the Salar del Carmen segment of the Atacama Fault System (northern Chile): Fault scarp morphology and knickpoint analysis

Oktawian Ewiak[1], Pia Victor[1], and Onno Oncken[1]

[1]Department of Geodynamics, GeoForschungsZentrum Potsdam, Potsdam, Germany

Abstract This study presents a new geomorphological approach to investigate the past activity and potential seismic hazard of upper crustal faults at the Salar del Carmen segment of the Atacama Fault System in the northern Chile forearc. Our contribution is based on the analysis of a large set of topographic profiles and allows extrapolating fault analysis from a few selected locations to distances of kilometers along strike of the fault. We detected subtle changes in the fault scarp geometry which may represent the number of paleoearthquakes experienced by the structure and extracted the cumulative and last incremental displacement along strike of the investigated scarps. We also tested the potential of knickpoints in channels crossing the fault scarps as markers for repeated fault rupture and proxies for seismic displacement. The number of paleoearthquakes derived from our analysis is 2–3, well in agreement with recent paleoseismological investigations, which suggest 2–3 earthquakes ($M_w = 6.5–6.7$) at the studied segments. Knickpoints record the number of events for about 55% of the analyzed profile pairs. Only few knickpoints represent the full seismic displacement, while most retain only a fraction of the displacement. The along-strike displacement distributions suggest fault growth from the center toward the tips and linkage of individual ruptures. Our approach also improves the estimation of paleomagnitudes in case of multiple fault rupture by allowing to quantify the last increment of displacement separately. Paleomagnitudes calculated from total segment length and the last increment of displacement ($M_w = 6.5–7.1$) are in agreement with paleoseismological results.

1. Introduction

The investigation of fault-generated landforms such as fault scarps is a common technique used to study fault evolution, the recurrence of faulting events, and the probability and severity of future earthquakes [e.g., *Wallace*, 1977; *Nash*, 1980; *Hanks et al*., 1984; *Andrews and Hanks*, 1985; *Avouac and Peltzer*, 1993; *McCalpin*, 2009]. Historical and instrumental records alone are sometimes insufficient to characterize seismogenic faults [e.g., *McCalpin*, 2009] as demonstrated by many devastating earthquakes in the past decade that occurred on faults, which have not recorded any large historic events, including the 2003 $M_w = 6.6$ Bam earthquake in Iran [*Fu et al*., 2004], the 2005 $M_w = 7.6$ Kashmir earthquake in Pakistan [*Kaneda et al*., 2008], and the 2008 $M_w = 8.0$ Wenchuan earthquake in China [*Liu-Zeng et al*., 2009]. Paleoseismological trenching campaigns provide detailed information about the recurrence and magnitudes of prehistoric earthquakes [e.g., *Kumar et al*., 2006; *Cortés et al*., 2012; *Madugo et al*., 2012]. However, trenching of large fault systems is an extensive effort and spatially limited to few selected locations along the fault. Geomorphological analyses of fault scarps are widely accepted to determine cumulative displacement or approximate the age of a fault scarp for single fault ruptures [e.g., *Bucknam and Anderson*, 1979; *Avouac and Peltzer*, 1993; *Mattson and Bruhn*, 2001]. *Wallace* [1980, 1984] proposed gradient changes, i.e., slope breaks, in the morphology of fault scarps as indicators for multiple rupture events along a fault.

In our study, we use a set of densely spaced, high-resolution topographic profiles to detect slope breaks and to test their application as geomorphic markers for repeated rupture at the Salar del Carmen segment of the Atacama Fault System. In addition, we use the fault scarp morphology to quantify the cumulative and last incremental displacement along strike of the selected fault scarps. The observation that may knickpoints in the study area are restricted to the immediate vicinity of the fault scarps led to the idea of testing the potential of knickpoints as additional markers for the number of surface-rupturing events and potential seismic displacement. Based on mapped surface rupture lengths and measured vertical displacements, we also estimate magnitudes of possible paleoearthquakes using a set of empirical regressions [*Wells and*

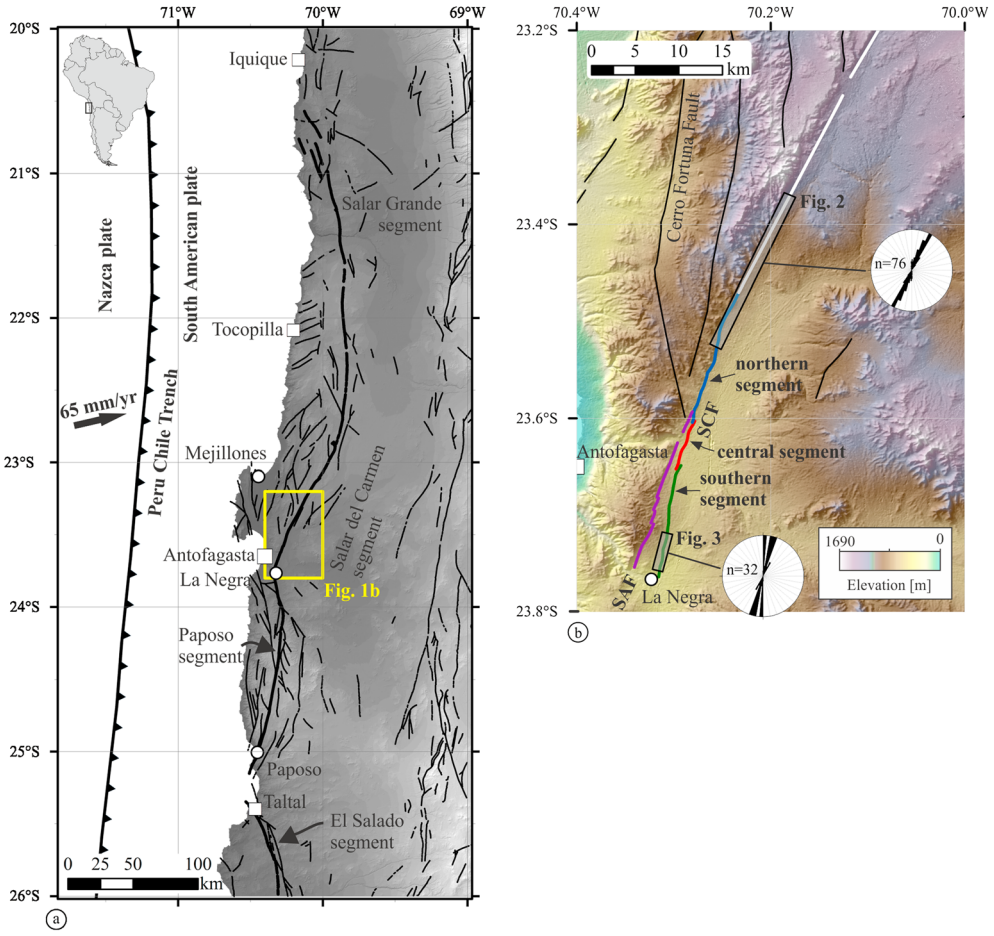

Figure 1. (a) Regional scale geometry of the AFS between Iquique and Taltal (modified after *Reutter et al.* [1994]). Bold lines denote main segments of the AFS. The barbed line to the west of the coastline marks the location of the trench. The black arrow represents the convergence vector [*Norabuena et al.*, 1999]. (b) Color-coded topographic map at the latitude of the SCF. The SAF is marked by the purple line. Green, red, and blue traces denote active segments of the SCF (modified after *González et al.* [2003]). The white line represents the continuation of the AFS north of the SCF. Elevation data are based on the ASTER Global Digital Elevation Map data set (asterweb.jpl.nasa.gov/gdem.asp). The rose plots show strike directions of mapped fault traces within the black boxes.

Coppersmith, 1994; *Stirling et al.*, 2002]. Our investigation aims at testing the applicability of the aforementioned geomorphic features to (a) quantify the number of surface-rupturing events along the strike of the selected fault system, (b) extract the vertical displacement pattern, and (c) derive reliable estimates for paleomagnitudes, which is a persisting challenge in paleoseismology [e.g., *McCalpin*, 2009].

Paleoseismological trenches along the investigated fault segments serve as an additional, independent reference for the number of events on the studied segments and the corresponding paleomagnitudes. In combination with existing results from paleoseismological trench logs [*González et al.*, 2010; *Robinson et al.*, 2011; *Cortés*, 2013], we show that our analysis of geomorphic markers is a valuable complement to trenching campaigns that provides additional information along strike of the target faults. We demonstrate that only a few trenches are necessary to confirm the results derived from the geomorphic record. In addition to presenting a well-suited geomorphological approach to assess the multiple rupture history of a complex fault zone, our contribution adds valuable knowledge regarding the past activity of the Salar del Carmen segment.

2. Geological Background

2.1. The Atacama Fault System

The Atacama Fault System (AFS) is the dominant structural element of the northern Chilean Coastal Cordillera (Figure 1a). It extends for over 1000 km from the cities of Iquique (21°S) to La Serena (30°S) and consists of three

arcuate trench-parallel segments. The large-scale geometry of the AFS was established in Late Jurassic–Early Cretaceous times, contemporaneous with the activity of the former magmatic arc. The AFS most likely originated as a trench-linked sinistral strike-slip fault system [e.g., *Naranjo et al*., 1984; *Naranjo*, 1987; *Thiele and Pincheira*, 1987; *Hervé*, 1987a; *Scheuber and Andriessen*, 1990; *Scheuber and Reutter*, 1992; *Brown et al*., 1993; *Cembrano et al*., 2005; W. J. Arabasz Jr., Geological and geophysical studies of the Atacama fault zone in northern Chile, unpublished PhD thesis, California Institute of Technology, 1971]. At present, the AFS extends over the onshore portion of the forearc along the Perú-Chile subduction zone (Figure 1a) and is located above the coupling zone of the subduction interface between the South American Plate and the Nazca Plate [e.g., *Tichelaar and Ruff*, 1991; *Delouis et al*., 1996; *Buske et al*., 2002]. Recent convergence based on GPS data is characterized by a vector of 075° and a rate of approximately 65 mm/yr [e.g., *Norabuena et al*., 1999]. Evidence for young reactivations of various segments of the AFS in Cenozoic times has been described in numerous studies [e.g., *Hervé*, 1987b; *Naranjo*, 1987; *Armijo and Thiele*, 1990; *Delouis et al*., 1998; *González et al*., 2003, 2006; *González and Carrizo*, 2003; *Loveless*, 2007; *Allmendinger and González*, 2010; W. J. Arabasz Jr., unpublished PhD thesis, 1971]. W. J. Arabasz Jr. (unpublished PhD thesis, 1971) suggested that vertical movements have taken place since Miocene times. Most authors agree on a reactivation as a steep normal fault in Tertiary times, whereas the exact timing of reactivation and the recent evolution of the AFS are a matter of debate. Due to its location in the hyperarid Atacama Desert [e.g., *Hartley and Chong*, 2002; *Dunai et al*., 2005], characterized by extremely low erosion rates of about 1 m/Ma [*Kober*, 2005; *Schlunegger et al*., 2006], the AFS is a prime target for the study of geomorphic markers.

2.2. The Salar del Carmen Fault

The most active fault branches of the AFS in the study area (Figure 1b) offset the eastern piedmont of the Coastal Cordillera east of the city of Antofagasta [e.g., *González et al*., 2003]. At a local scale, in the Salar del Carmen region, the AFS consists of two main approximately parallel fault strands (Figure 1b). The Sierra del Ancla Fault (SAF), which is a bedrock-cutting fault, marks the eastern boundary of the Coastal Cordillera ranges. It extends for more than 23 km from La Negra to 10 km north of the Salar del Carmen [*González et al*., 2003]. The Salar del Carmen segment, mostly referred to as Salar del Carmen Fault (SCF), is a N to NNE striking structure, approximately 60 km long (Figure 1b), which dissects Quaternary alluvial fan deposits.

González et al. [2003] subdivided the SCF in three segments (Figure 1b) connected by relay ramp structures. The northernmost segment strikes N15°E and extends for more than 30 km. The central, N15°E striking segment outlines the western boundary of the Salar del Carmen basin and is only 6 km long. The southernmost segment is located between the Salar del Carmen basin and La Negra. All three segments display mainly east-facing, west-side-up fault scarps [*González et al*., 2003, 2006]. *González and Carrizo* [2003] reported piedmont, multiple, and composite fault scarps at the SCF dominated by debris slopes and retreating free faces. The abandoned fan surface west of the SCF is dissected by a well-developed drainage system consisting of numerous channels, gullies, and small rills, which crosscut the active fault scarp.

The material for the construction of the alluvial fans has been eroded from the Coastal Cordillera ranges [e.g., *Hartley et al*., 2005]. The main lithologies are volcanic rocks, volcanogenic sedimentary rocks, sedimentary rocks, and intrusive rocks of Jurassic-Cretaceous ages [e.g., *Scheuber and Andriessen*, 1990; *Cortés*, 2013]. These include several formations, e.g., the volcanic La Negra Formation, the sedimentary Caleta Coloso Formation, and the marine sediments of the El Way Formation [e.g., *Espinoza*, 1983; *Scheuber and Andriessen*, 1990; *Cortés*, 2013].

Two main generations of alluvial fans have been identified in the study area (Figure 1b): (a) old inactive fans forming the upper surface west of the SCF and, where not eroded or covered by younger deposits, parts of the lower surface east of the SCF, and (b) young, recently active fans deposited immediately east of the SCF by ephemeral streams dissecting the fault scarp. Alluvial fans belonging to the older generation mainly consist of gravel, sand, and fine-grained material, and contain salt and gypsum horizons. They have been deposited by episodic sheet flow events [*Hartley et al*., 2005]. The thickness of these alluvial deposits is at least 20 m [*González and Carrizo*, 2003]. The age of the inactive fan surface, as determined by a single data point, is 424 ± 151 ka [*González et al*., 2006]. The younger fans are considered to be active during episodic rain events [e.g., *Vargas et al*., 2000, 2006]. *González et al*. [2006] reported a reactivation of these fans during the last heavy rain event of 1991. The fault scarps analyzed in this study are crosscutting alluvial fan material with approximately horizontal bedding planes. Over the course of our field campaigns, we did not observe any exposures of the underlying

bedrock along the studied fault segments. Therefore, we exclude major lithological contrasts and assume that the analyzed geomorphic features result solely from the interplay of faulting and erosion.

Evidence for young reactivations of the SCF has been reported in several studies analyzing fault scarps crosscutting young Quaternary deposits, suggesting active faulting [e.g., *Delouis et al*., 1998; *González et al*., 2003, 2006; *González and Carrizo*, 2003; *Allmendinger and González*, 2010]. Fresh surface ruptures and abundant open tension cracks also indicate recent activity [*Loveless et al*., 2005, 2009; *Loveless*, 2007; *Shirzaei et al*., 2012]. According to *González et al*. [2003], normal faulting must have been active during the construction of the eastern piedmont of the Coastal Cordillera. By dating quartz fragments from inactive fan surfaces using ^{21}Ne, *González et al*. [2006] obtained 424 ± 151 ka as upper limit for activity of the SCF. *González and Carrizo* [2003] used 21 fault scarp profiles measured along 45 km of the total length of the SCF to quantify the cumulative vertical displacements (2.1–8.9 m). They calculated morphological ages between 4 ka and 400 ka, strongly dependent on the diffusion constant used in the scarp degradation modeling.

In spite of numerous reports of fault reactivation, detailed paleoseismological investigations and the potential for seismic surface-rupturing events at the AFS are a very recent topic [*González et al*., 2010; *Robinson et al*., 2011; *Cortés*, 2013]. *Robinson et al*. [2011] reported 3–4 large slip events on the SCF in the last 13 ka, while *Cortés* [2013] documented at least two paleoearthquakes with magnitudes of $M_w = 6.5–6.7$ in the past 12 ka. These results demonstrate that the interpretation of fault evolution along a 60 km long segment of the AFS is difficult if based only on localized results from a limited number of trenches.

2.3. Fault Segments Analyzed in This Study

For our study we have chosen two active segments of the SCF (Figure 1b) to test geomorphological techniques for the identification of multiple rupture events. The following constraints have been mandatory for the segment choice: (a) a well-localized fault scarp with at least locally preserved free faces, (b) clear segments limited by tip points, and (c) the presence of paleoseismological trenches providing additional information on the fault segments [*González et al*., 2010; *Robinson et al*., 2011; *Cortés*, 2013]. These chosen segments dissect and offset alluvial fans of the eastern piedmont of the Coastal Cordillera. They are separated by a distance of approximately 26 km, permitting the analysis of variations in displacement distribution along strike, fault slip accumulation, and the number of rupturing events.

The northern fault segment, referred to as Cumbre Jequier segment in this publication (CJS, Figure 2), is located in the central part of the northern segment proposed by *González et al*. [2003, 2006] (Figure 1b).The southern limit of this dip-slip fault is located just south of Ruta B-400, where the fault scarp splits up into several traces, terminating in strongly cracked bedrock. The northern limit is marked by a major gap of 2.3 km. The segment as defined by the aforementioned limits can be traced over a total length of 19 km (Figure 2a). Based on detailed field and aerial mapping, we have identified 76 individual surface ruptures ranging from a few tens of meters to 1796 m. Fault scarps strike between N15°W and N38°E, based on simplified traces connecting the tip points. Calculation of linear directional mean yielded an average strike of N25°E (see rose plot in Figure 1b). We also identified short scarps with lengths of 10–50 m, striking oblique (N-S) to the main fault scarp segments (Figures 2b and 2c), which may represent Riedel shears suggesting minor strike-slip components. Retreating free faces have been preserved locally, but have been eroded in most cases. Remnants of the original fault planes are mainly preserved along portions of the fault scarps, which are indurated with salt and gypcrete [e.g., *Loveless et al*., 2005], and thus more resistant to erosion.

The southern segment, which is referred to as La Negra segment (LNS, Figure 3), is located north of La Negra (Figure 1b). Its southern termination is located in a strongly cracked area north of Ruta 28. We defined the location of the southern tip point where the fault scarp splits into several splays, and the measured offset decreases to zero (Figure 3a). The northern tip point lies on an abandoned fault surface 3300 m to the north, where the surface expression of the fault terminates in a well-defined tip point. Based on field and aerial mapping, we determined 32 individual subsegments over the extension of the LNS, joined by small-scale step overs. Locally, individual subsegments may be separated by small-scale gaps of a few tens of meters. However, the pronounced parallelism of these subsegments and the geomorphic appearance hint to a single fault segment (Figure 3a). The length of the individual subsegments ranges from 27 m to 883 m. Fault scarps strike between N2°W and N29°E based on simplified traces connecting the tips of each individual subsegment. Calculation of linear directional mean yielded an average strike of N12°E (see rose plot in

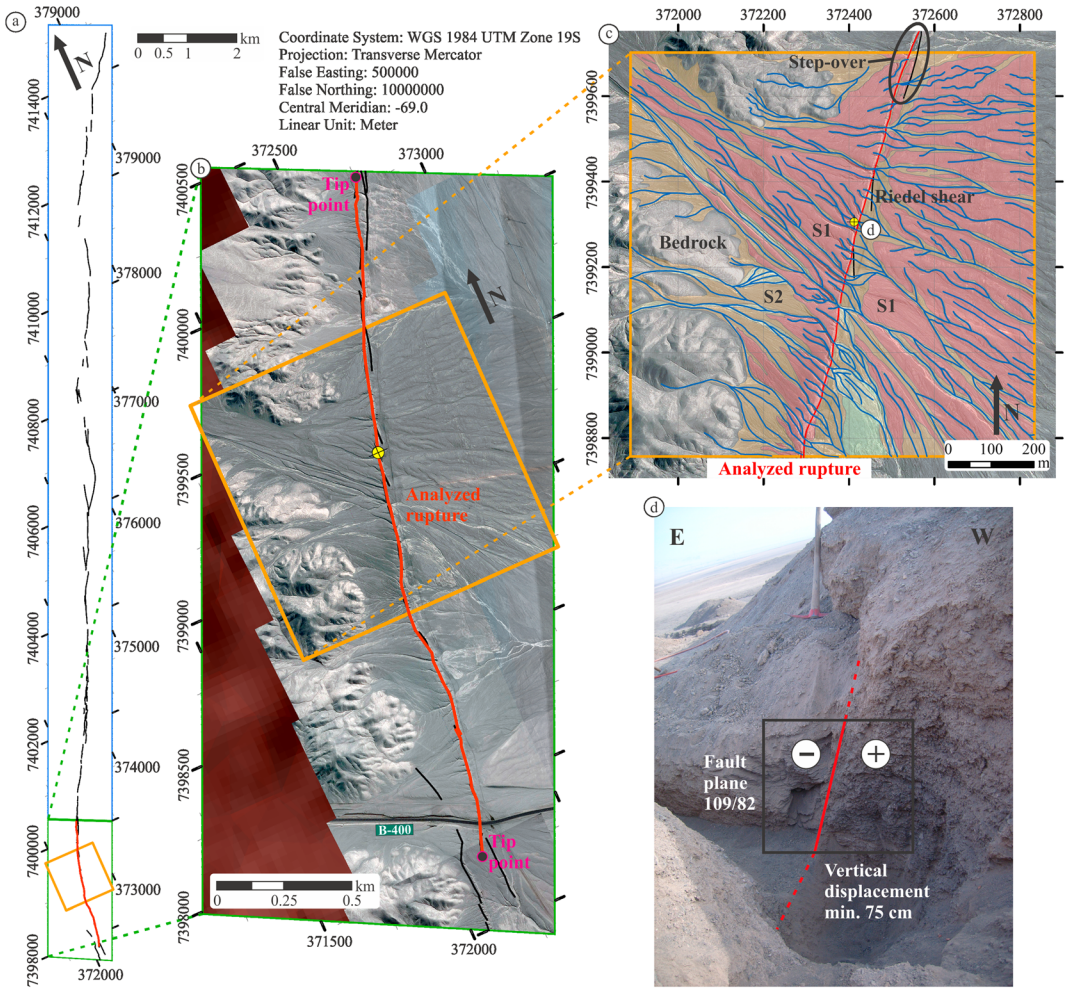

Figure 2. (a) Overview of the Cumbre Jequier segment showing the entire fault segment (19 km). Fault traces are marked by black lines. The red line represents the analyzed subsegment. See also Figure S1 for a detailed aerial view of the fault segment. (b) Detailed view of the analyzed subsegment. Tip point locations based on field observations are marked with dots. The yellow circle refers to the field photograph shown in Figure 2d. (c) Map of the dominant fan generations and the channel system (modified after *Cortés* [2013]). Indices S1 and S2 mark fan surfaces, with S1 being the older one. (d) Field photograph showing the fault in a trench at a creepmeter installation site [*Victor et al.*, 2012].

Figure 1b). As with the case of the CJS, remnants of the original fault planes are only preserved along indurated portions of the fault scarps.

3. Geomorphic Markers as Proxies for Fault Displacement

Studies of fault-generated landforms such as fault scarps provide information about the fault forming process, the recurrence of faulting events, and the fault evolution through time [e.g., *Wallace*, 1977; *Nash*, 1980; *Hanks et al.*, 1984; *Andrews and Hanks*, 1985; *Avouac and Peltzer*, 1993; *McCalpin*, 2009]. The initial morphology of a fault scarp depends on the style of faulting, the amount of displacement, and the material properties, and may be significantly complicated by splay faults, or by the occurrence of multiple offsets along the same fault plane. The main types of normal fault scarps and their components are depicted in Figure 4. Evidence for multiple displacements on a single fault trace can be obtained from (a) several pronounced slope breaks in fault scarp profiles [e.g., *Wallace*, 1980, 1984], (b) benches or terraces along channels and gullies that dissect the fault scarp, (c) a cumulative scarp height exceeding the maximum surface offset for an individual surface-rupturing event, and (d) larger displacement of older deposits than younger deposits [*Wallace*, 1977]. More recent studies [*Mayer*, 1984; *Avouac and Peltzer*, 1993; *Mattson and Bruhn*, 2001] have confirmed the importance of slope breaks in scarp profiles as indicators for repeated faulting and successfully identified multiple faulting events.

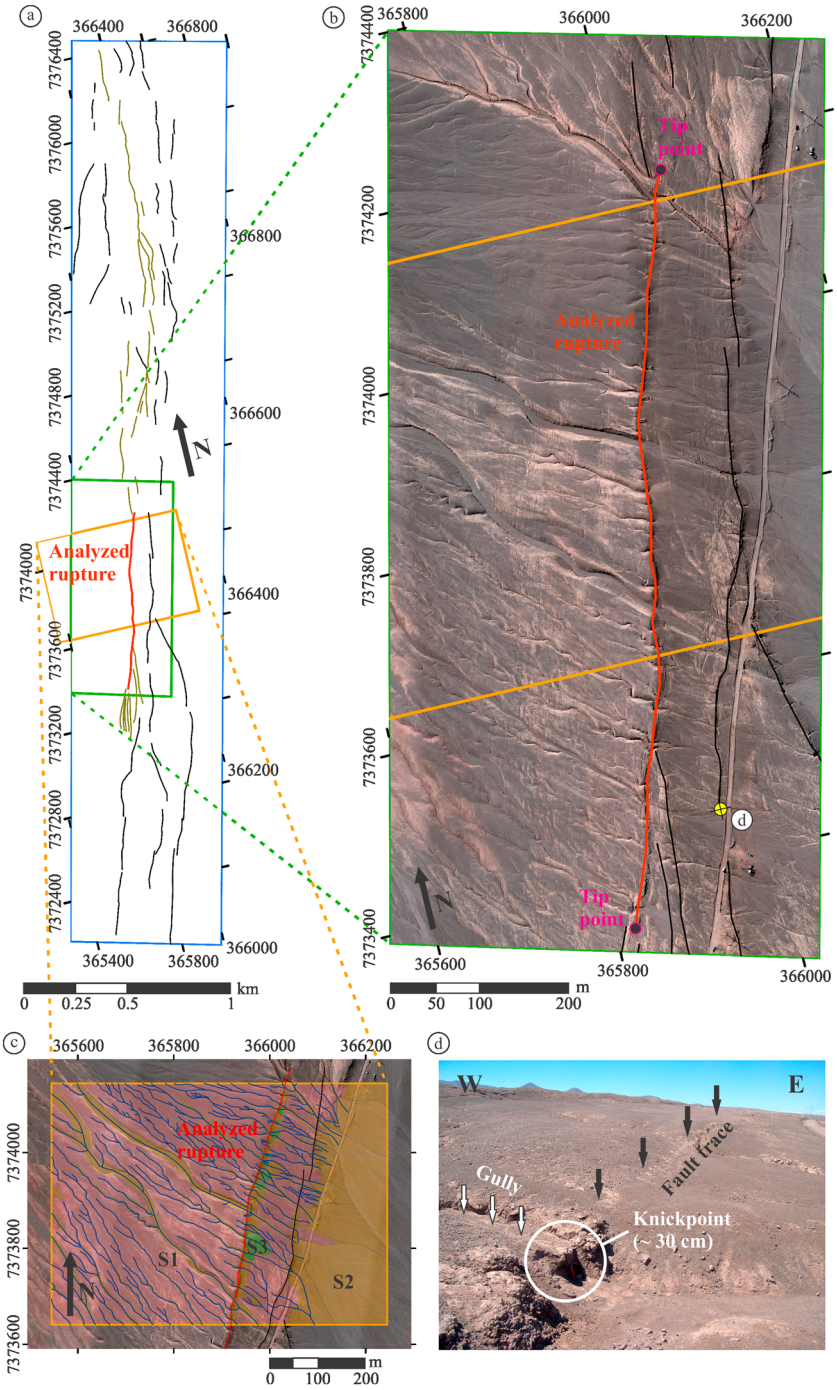

Figure 3. (a) Overview of the La Negra segment. Fault traces are marked by lines. Olive green lines represent ruptures with similar morphological characteristics, which have most likely ruptured in a single event. The red line represents the analyzed subsegment. See also Figure S2 for a detailed aerial view of the fault segment. (b) Detailed view of the analyzed subsegment and its tip points. The yellow circle refers to the field photograph in Figure 3d. (c) Map of the dominant fan generations and the channel system (modified after *Cortés* [2013]). Index S1 marks the oldest fan surface. S2 and S3 represent younger fan generations. (d) Field photograph of a knickpoint located directly at a small fault scarp.

Another alternative geomorphic marker tested in this study are knickpoints (Figures 3d and 4a), which have been originally described by *Gilbert* [1895] and *Penck* [1924] as steep or convex reaches in longitudinal river profiles. Later publications defined knickpoints as abrupt breaks in slope in a longitudinal stream profile or as discrete, steep reaches, which create a local convexity in the channel profile [e.g., *Gardner*, 1983; *Crosby*

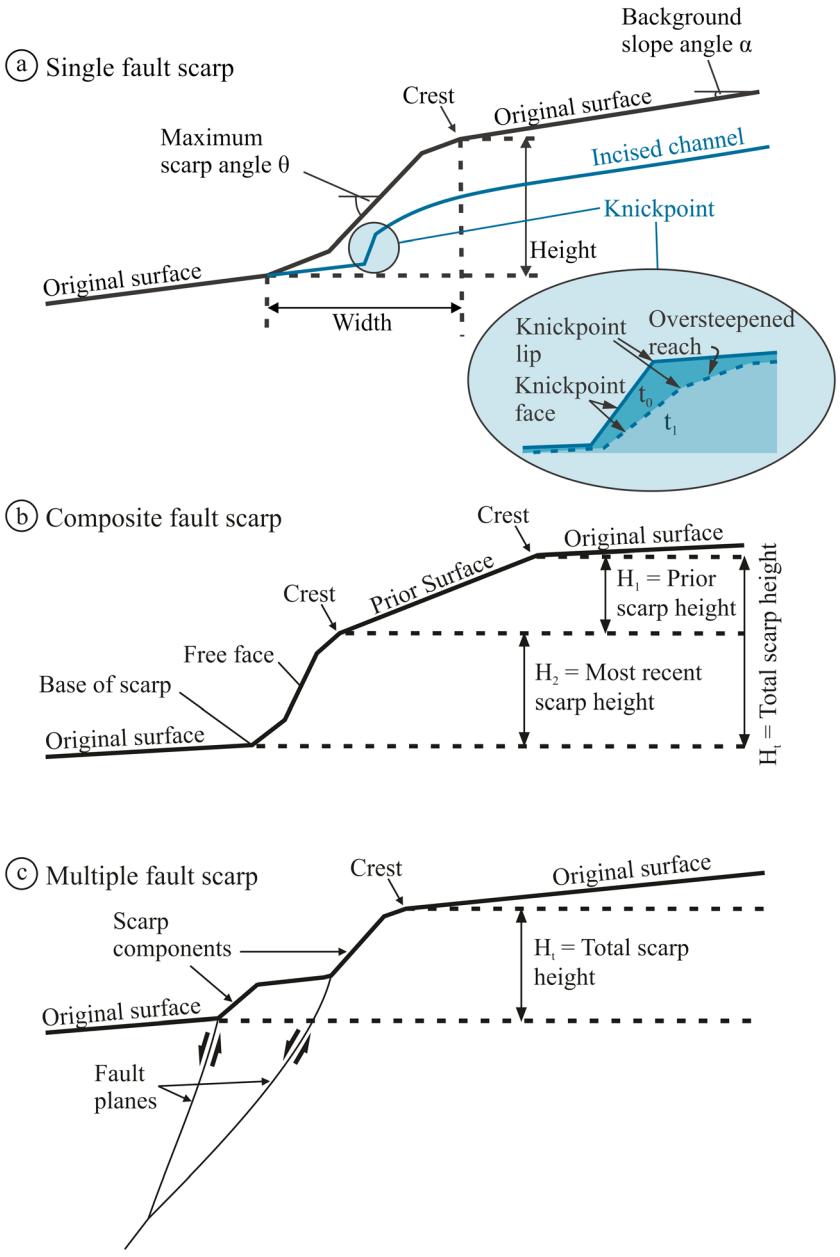

Figure 4. Fault scarp types modified after *Mayer* [1984]. (a) Single or piedmont fault scarp. Several components can be distinguished based on the slope angle (θ): free face (angle > 45°), debris slope (30°–45°), and wash slope (typically 5°–10°). The inset shows the general morphological components of a knickpoint [e.g., *Gardner*, 1983]. The knickpoint degrades between time steps t_0 and t_1. (b) Composite fault scarp resulting from multiple ruptures along the same fault plane. Total scarp height $H_t = H_1 + H_2 + \ldots + H_n$. (c) Multiple fault scarp resulting from slip along multiple fault planes. The total scarp height equals the sum of its components.

andWhipple, 2006; *Berlin and Anderson*, 2007]. Perturbations leading to knickpoint formation are manifold including sudden or stepwise changes in base level [*Penck*, 1924; *Begin et al.*, 1981; *Gardner*, 1983; *Whipple and Tucker*, 1999; *Hassan and Klein*, 2002], lithological variations [*Holland and Pickup*, 1976], or preexisting geological structures [*Miller*, 1991; *Weissel and Seidl*, 1997]. However, the existence of knickpoints which appear to be directly related to tectonic perturbations has been described in various publications [e.g., *Litchfield et al.*, 2003; *Yanites et al.*, 2010; *Huang et al.*, 2013].

Our study integrates the results derived from detailed mapping of surface ruptures and the analysis of fault scarp morphology and knickpoints located in crosscutting channel systems. We compare the results of

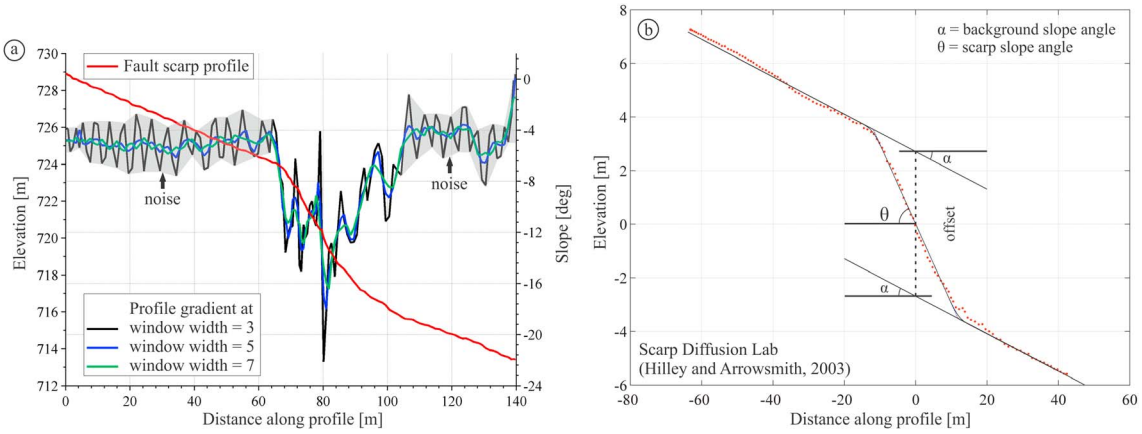

Figure 5. Methodology for measurement of vertical displacement, detection of slope breaks, and identification of knickpoints. (a) Identification of slope breaks in profile gradients calculated with sliding windows of varying size. The example profile shown represents a composite fault scarp with three pronounced slope breaks. (b) Scarp Diffusion Lab [*Hilley and Arrowsmith*, 2003]. After fitting a line oriented at the background angle α to the profile data, the surface offset and the scarp slope angle θ are measured at the center of the scarp.

both knickpoint analysis and fault scarp morphology analysis to test the potential of the former as a complementary/alternative proxy to detect fault displacements.

4. Methods

4.1. Data Acquisition and Processing

We used a densely spaced set of 203 topographic profiles to investigate the number of surface-rupturing events and the spatial pattern of displacement along the two selected fault segments (Figures 2b and 3b). The data comprise topographic profiles oriented perpendicular to the fault scarps (109) and longitudinal profiles of gullies (94) incised into the alluvial fans and crosscutting the fault scarps nearly perpendicular to the fault strike.

Differential GPS measurements were carried out using a Leica GNSS 1200+ System with an ATX1230GG Smart Antenna as rover and an AX1203+ Antenna as reference antenna. The reference antenna was set up on stable ground, while the roving antenna was mounted on a backpack. Sampling frequencies for both antennas were set to 1 Hz equivalent to approximately 1–2 data points/m on the fan surface and 3–4 data points/m at the fault scarps for the roving antenna.

To ensure consistency between profile data sets that have been acquired during a series of field campaigns, all profiles were referenced to a single reference antenna position calculated using Precise Point Positioning (PPP). Positions calculated with PPP using precise ephemeris and clock correction data provided by NASA [http://www.gdgps.net] were distributed over an area with a radius of ~1 cm. Subsequent baseline processing was carried out using Leica's Geo Office software (V. 7.0). The quality of the processed positions was examined using the RMS of the standard deviations of the calculated horizontal and vertical point coordinates. All points used for profile creation showed instrumental accuracy of 1 cm or better. Points with a lower accuracy were dismissed from further analysis. Although the instrumental error of the final data sets was very low, we used a more conservative threshold to compensate for random errors inherent to the measurement method. For the quantitative analysis of fault scarp morphology and knickpoints we considered only features with a height of at least 7.5 cm.

4.2. Detection of Individual Faulting Events

The detection of slope breaks and knickpoints in topographic profile data requires the computation of the gradient, i.e., the first derivative, along the acquired profiles and the detection of gradient changes. For the detection of slight gradient changes in the degraded portion of the fault scarp it is essential to apply a methodological approach that is as sensitive as possible but, on the other hand, does not overinterpret gradient changes.

We chose a sliding window approach to calculate the gradient along each elevation profile. By varying the size of the sliding window, we were able to optimize the signal-to-noise ratio. Larger window sizes reduce the noise, while small window sizes preserve slight changes in profile gradient (Figure 5a). The slope gradients

were computed using the Matlab function Movingslope [*D'Errico*, 2007]. The calculation consists of two subsequent steps for each window position: (a) a polynomial regression model is fit to the data inside the sliding window; (b) the model is differentiated to compute the gradient. We chose a linear model, so the result equals the gradient of the profile in down-slope direction. During the course of our work we developed a suite of functions allowing for automatized import of profile data, data organization and parsing, computation of gradient for a predefined selection of window sizes, and results output. The most appropriate window sizes for detection of slope breaks in our fault scarp profiles range from three to seven data points equivalent to a profile distance of approximately 1.5 to 3.5 m or 0.75 to 1.75 m at the more densely sampled fault scarp. The positions of slope breaks in the elevation profiles are marked by steep troughs in the calculated profile gradient (Figure 5a). For an ideal single-rupture fault scarp, the onset of the trough marks the crest of the fault scarp. The end of the trough marks the return to the background slope angle of the alluvial fan. The maximum absolute value in gradient marks the center of a (symmetric) fault scarp. In case of composite fault scarps, each consecutive event rejuvenates the fault scarp and results in an additional slope break in the fault scarp profile. The most recent events are documented by steep free faces or slightly degraded parts of the fault scarp, which have not been significantly modified by erosion [e.g., *Wallace*, 1984]. We note that we considered only slope breaks in the upper part of the scarp to infer the number of faulting episodes as the lower part of the fault scarp is subject to depositional processes and the formation of a debris slope covering the original morphology. The described methodology was checked by ground truthing for selected profiles. The sensitivity of our approach has been additionally tested using synthetic elevation profiles (see supporting information).

A similar approach has been used to detect knickpoints in longitudinal gully profiles. To ensure completeness of the knickpoint data set, the gully profiles were additionally examined visually for smaller features and knickpoint positions mapped in the field were added to the final data set if missing. Subsequently, we compared the spatial distribution of the number of slope breaks with the number of knickpoints detected in adjacent gully profiles to test if the investigated markers can be used to estimate the number of faulting events responsible for fault scarp formation.

4.3. Extraction of Fault Scarp Displacement and Knickpoint Height

The extraction of fault scarp heights has been conducted using two independent approaches. In a first step, we used the Matlab code Scarp Diffusion Lab (SDL) [*Hilley and Arrowsmith*, 2003] to measure cumulative surface offsets at the fault scarps. Prior to measurement, we fitted a line to the profile data and determined the far-field background angle α using the offset profile correction function (Figure 5b). Subsequently, we extracted the offset at the center of the fault scarp by reading the height difference between the lines defined by the best-fitting background angle α. In a last step, we also measured the maximum scarp slope angle θ, which can be used to classify fault scarp components as, e.g., the free face or the debris slope, based on their slope angles. The main advantages of this approach are (a) it takes into account the far-field background slope of the faulted deposits, and (b) it provides additional information on the maximum scarp slope angle θ. However, it has to be noted that it proved difficult to fit the background angle α properly to the profile data in case of composite and multiple fault scarps. A further limitation arises if the slope of the upper surface does not equal the slope of the lower surface as the offset profile correction function does only allow a single value for the background slope angle α. Another drawback of this approach is that it yields only the cumulative displacement not allowing to distinguish between increments in case of a multiple rupture history.

During the course of this study we developed an alternative method for surface offset measurements since we mainly encountered composite and multiple fault scarps (Figure 6) with differences in the upper and lower far-field slope angles. We derived the cumulative vertical displacement by using the position of slope breaks along profile distance ($X_{R1\text{-}1}$, $X_{R1\text{-}2}$, $X_{R2\text{-}1}$, $X_{R2\text{-}2}$, Figure 6c) to identify the onset and the end of the fault scarp and to extract the corresponding elevation values ($Z_{R1\text{-}1}$, $Z_{R1\text{-}2}$, $Z_{R2\text{-}1}$, $Z_{R2\text{-}2}$, Figure 6c). Subsequently, we calculated the individual elevation differences $\Delta Z_{R1} = Z_{R1\text{-}1} - Z_{R1\text{-}2}$, $\Delta Z_{R2} = Z_{R2\text{-}1} - Z_{R2\text{-}2}$, and their sum $\Delta cum = \Delta Z_{R1} + \Delta Z_{R2}$, which represents the cumulative displacement (CD).

Our approach also allows the extraction of the last displacement increment (LDI), which is recorded by the steepest part of the fault scarp and thus marked by a sharp break in gradient data. The extraction of LDI followed the same principle as for CD, but we did only consider the steepest, youngest part of the fault scarp. In addition to the measurement of cumulative and incremental displacement, our method permits to examine the overall trend and the fluctuations of the background angle α. It is applicable to all types of fault

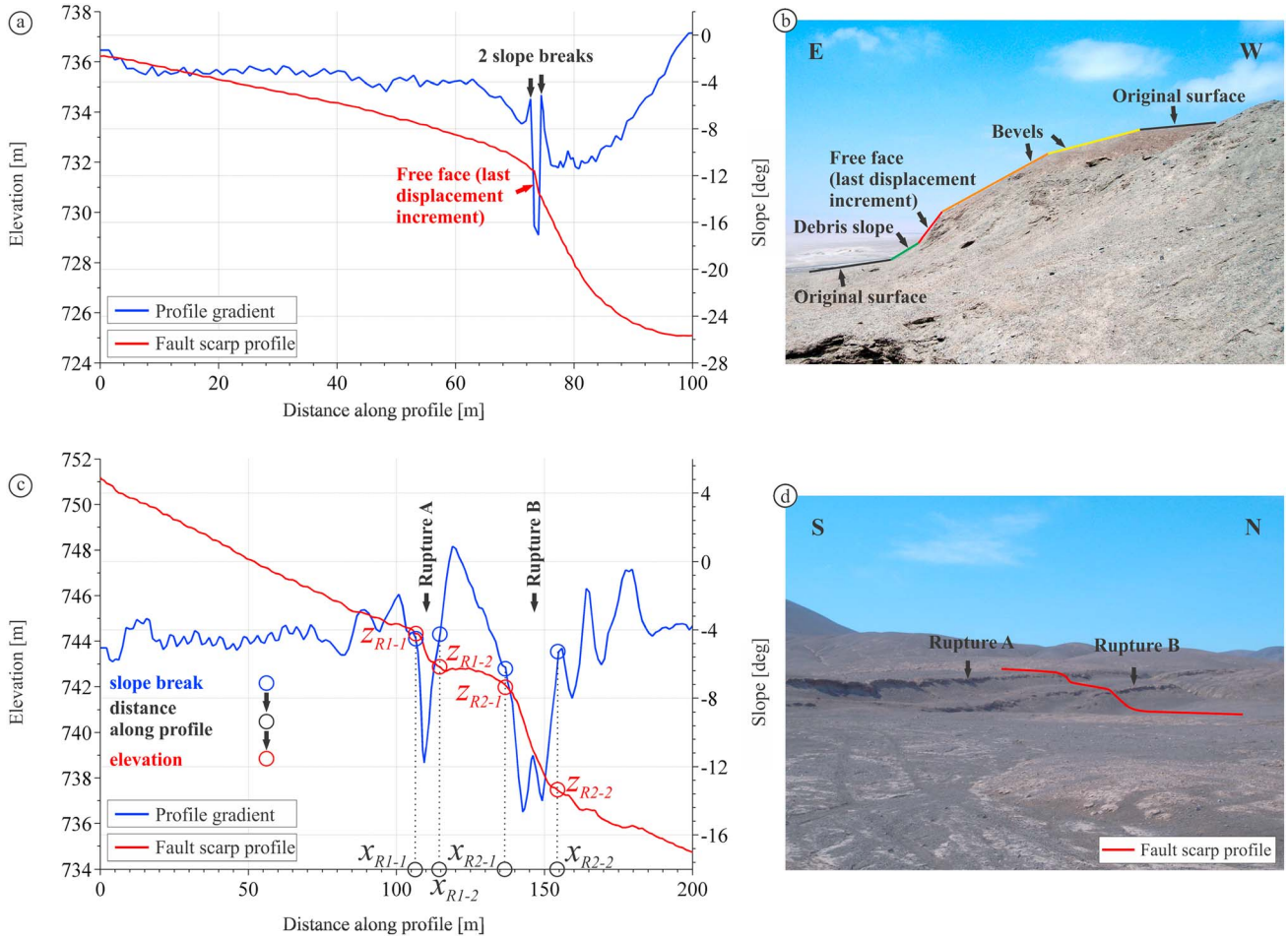

Figure 6. (a) Example profile of a composite fault scarp with two slope breaks. The last displacement increment is recorded by the steep free face. (b) Field photograph of a composite fault scarp with three slope breaks in its upper part. The free face represents the last displacement increment (LDI). (c) Example profile of a multiple fault scarp consisting of two ruptures. Measurement of cumulative displacement is based on the location of slope breaks ($X_{R1\text{-}1}$, $X_{R1\text{-}2}$, $X_{R2\text{-}1}$, $X_{R2\text{-}2}$). The cumulative displacement is approximated by the sum of surface offsets ($\Delta Z_{R1} = Z_{R1\text{-}1} - Z_{R1\text{-}2}$, $\Delta Z_{R2} = Z_{R2\text{-}1} - Z_{R2\text{-}2}$, $\Delta cum = \Delta Z_{R1} + \Delta Z_{R2}$). (d) Field photograph of the multiple fault scarp shown in Figure 6c.

scarps including composite and multiple fault scarps. We have to note that scarp height in fact represents surface offset and not necessarily the true vertical displacement. In case of fault dip angles $< 90°$, surface offset may underrepresent the true vertical displacement, depending on the background slope angle [e.g., *Cartwright et al.*, 1995; *McCalpin*, 2009]. For the average far-field slope angles at the analyzed fault scarps (4°–8°) and fault plane dips $> 80°$, the resulting underestimation of vertical displacement for a surface offset of 2 m is 2.5–5.0 cm. Therefore, we decided to use the surface offset as a direct approximation of the vertical displacement.

Knickpoint heights have been derived from field observations including manual height measurements and from longitudinal gully profiles. Extraction of knickpoint heights from profile data followed the same approach as for displacement at fault scarps. The onset and end of the trough in the calculated profile gradient were used to extract the corresponding elevation values along profile distance and to calculate the knickpoint height.

5. Results

5.1. General Characteristics of Fault Scarps in the Salar del Carmen Segment

The fault scarps at the CJS are characterized by a well-developed debris slope resting at an average angle of 26–27°. We identified both composite and multiple fault scarps (Figure 4). The maximum scarp slope angle θ_{max} exceeds 35° only where the free face is preserved. However, direct measurements in trenches showed

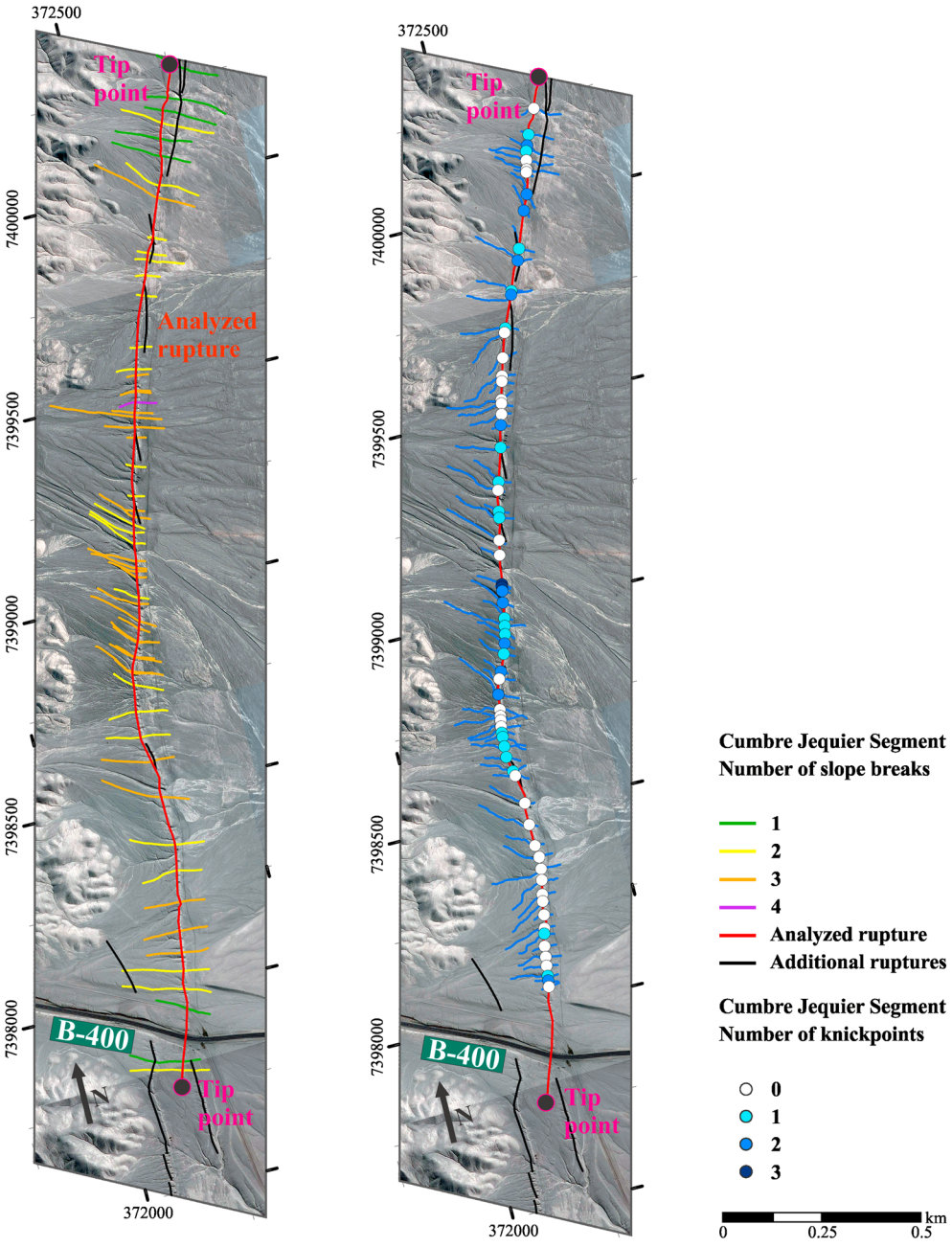

Figure 7. (left) Distribution of slope breaks along the analyzed fault scarp in the Cumbre Jequier segment. The red line marks the analyzed fault scarp, black lines denote additional surface ruptures, colored lines represent the profiles, with the number of slope breaks color-coded. Note the higher amount of slope breaks near the center of the fault segment. (right) Distribution of knickpoints along the analyzed fault scarp. Blue lines represent gully profiles, circles mark the location of knickpoints, colors refer to the number of knickpoints per profile.

fault plane dip angles of up to 82° (Figure 2d). The average maximum slope angle θ_{max} is about 26–27°, lower than commonly observed angles of repose (34°–37°) [e.g., *Wallace*, 1977; *Bucknam and Anderson*, 1979], indicating that the fault scarps have suffered some degradation. For detailed analysis of event numbers and quantification of displacement we picked a 2639 m long subsegment located in the southern part of the CJS (Figures 2a, 2b, 7, and 8).

For quantification of event numbers in the geomorphic record of the LNS, we chose an 883 m long, continuous fault scarp in the southern part of the fault segment (Figures 3a, 3b, 9, and 10). The maximum observed scarp

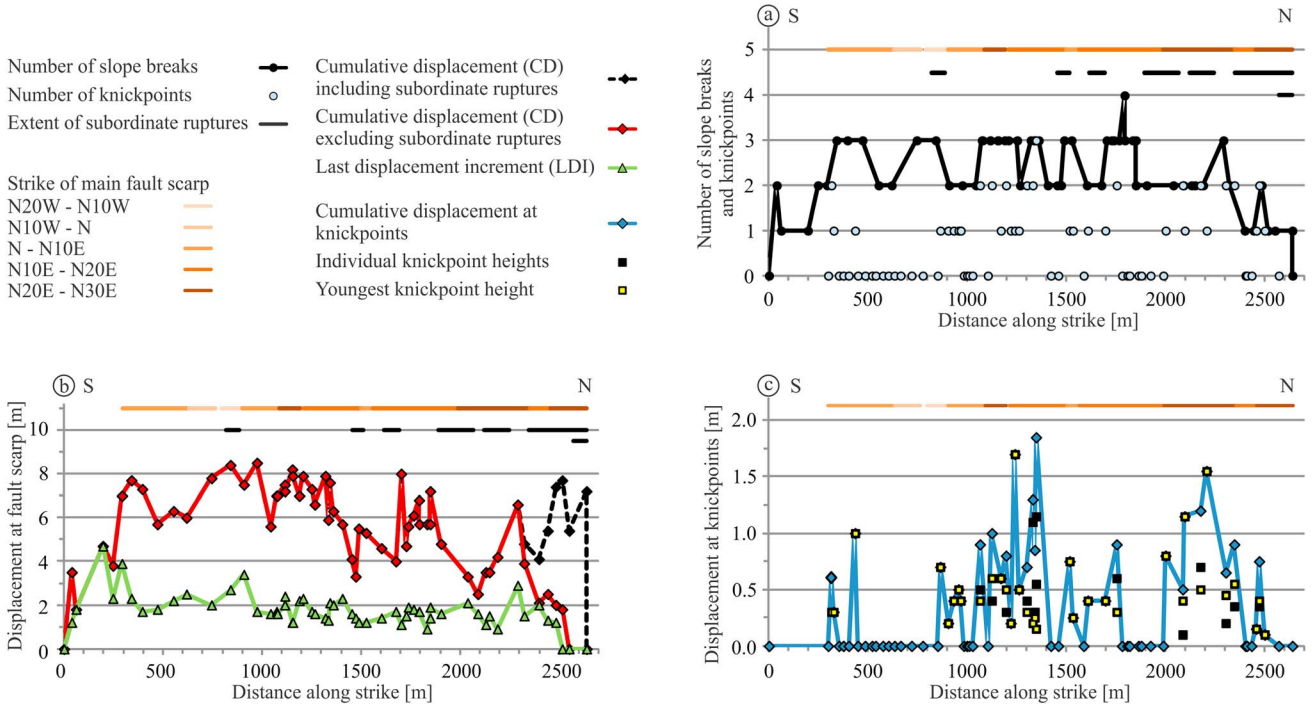

Figure 8. (a) Along-strike distribution of slope breaks and knickpoints in the Cumbre Jequier segment. The highest number of slope breaks correlates with the absence of subordinate ruptures. The number of knickpoints tends to be equal to or one less than the number of slope breaks in the fault scarp. Horizontal lines represent the extent of subordinate ruptures and the strike of the analyzed subsegment. (b) Along-strike displacement distribution. Local minima in CD tend to correlate with the occurrence of subordinate ruptures. The LDI appears more stable than CD. (c) Vertical displacement recorded at knickpoints. The solid line shows the cumulative vertical displacement. Black squares show individual knickpoint heights. Light squares mark the most recent knickpoints directly at the fault scarp.

slope angle θ_{max} was 70°, measured at a free face. Most fault scarps are characterized by a well-developed debris slope resting at an angle of ~35° or less. The average maximum scarp slope angle θ_{max} is 29°, indicating some degree of degradation. This slope angle is well in agreement with the average scarp slope angle measured in the CJS and suggests a similar degree of degradation for both study areas.

5.2. Estimates of Event Numbers Related to Fault Scarp Formation

Based on the analysis of 59 topographic profiles across the CJS fault scarp we were able to identify several slope breaks related to the development of the selected fault scarp and most likely indicative of multiple rupture episodes. The analyzed fault scarp displays more than one slope break along most of its length (Figures 7 and 8a). Twenty-three profiles display two abrupt breaks in gradient, whereas 28 profiles show three breaks in gradient. In one profile, located near the center of the segment, we detected four slope breaks. Based on these results, the fault scarp most likely experienced three individual faulting increments in the central part in its recent past. Profiles with two or less slope breaks tend to be located closer to the tips, suggesting that the fault has grown in length through time. Some exceptions of less than three slope breaks close to the central portion occur at bends, and in portions of the fault scarps, which are affected by subordinate segments or overlapping with other fault segments (Figures 7 and 8a). The events recorded in the scarp morphology compare well with the documented number of three to four events recorded in the paleoseismological trenches [*Robinson et al.*, 2011].

In case of the LNS, we analyzed 50 topographic profiles across the selected scarp, 38 acquired with Differential GPS, and 12 additional profiles extracted from data acquired with the Modular Airborne Camera System [*Lehmann et al.*, 2011; *Bucher et al.*, 2012]. The largest portion of the analyzed profiles (29 out of 50) contain two abrupt breaks in gradient, 17 profiles display three abrupt breaks (Figures 9 and 10a). Only two cases show four slope breaks. Near the northern tip, the number of detected slope breaks decreases to one. The distribution of slope breaks suggests a composite fault scarp resulting from repeated surface-rupturing events along the same fault plane, with three events preserved in the center of the fault scarp. Similar to the CJS,

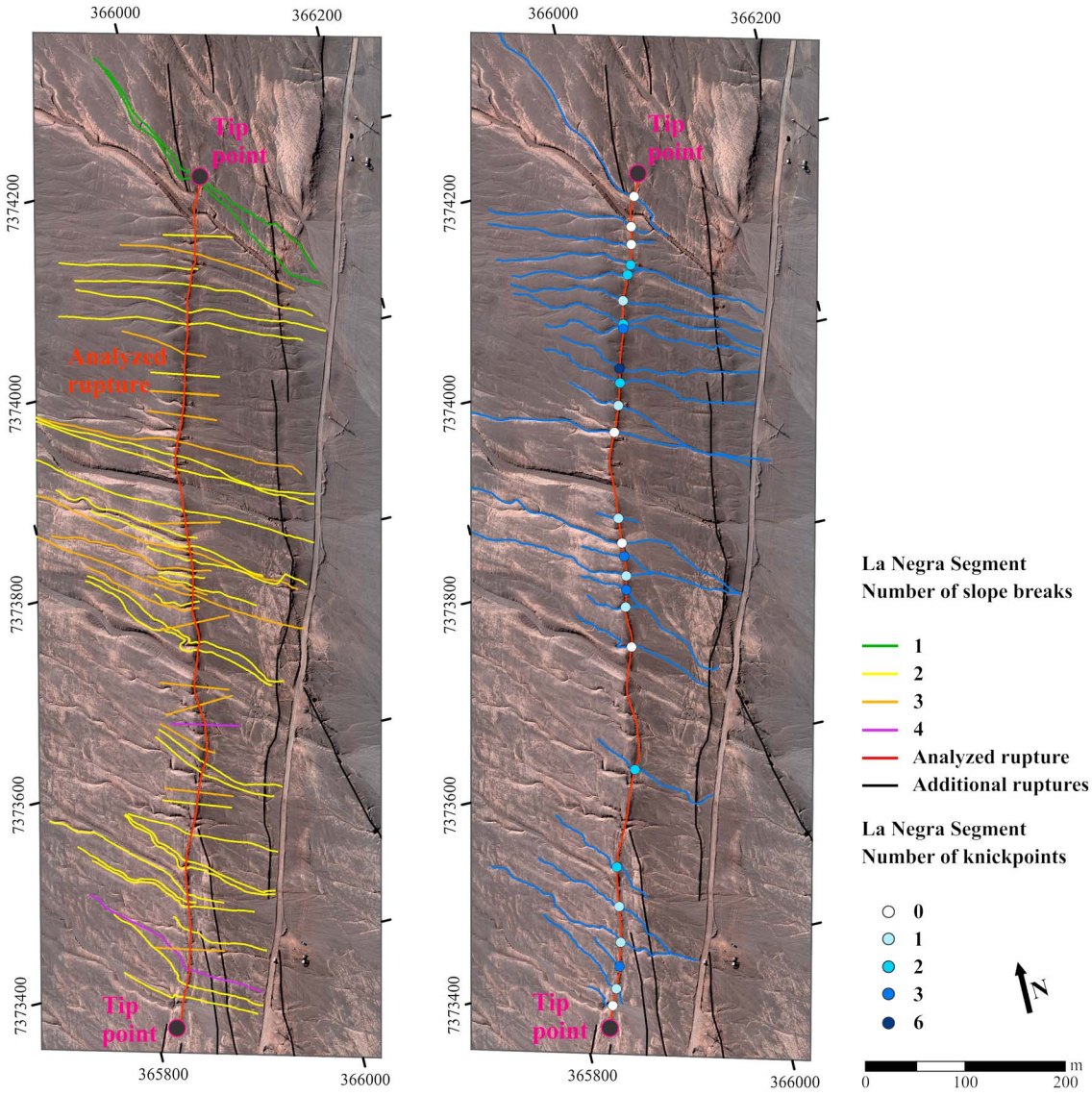

Figure 9. (left) Distribution of slope breaks along the analyzed fault scarp in the La Negra fault segment. The red line marks the analyzed fault scarp, black lines denote additional surface ruptures, colored lines represent the profiles, with the number of slope breaks color-coded. (right) Distribution of knickpoints along the analyzed fault scarp. Blue lines represent gully profiles, circles mark the location of knickpoints, colors refer to the number of knickpoints per profile.

the number of events preserved in the fault scarp morphology compares well with three to four events observed in paleoseismological trenches [*Robinson et al.*, 2011].

5.3. Cumulative and Incremental Displacements From Slope Breaks

We analyzed the displacement pattern along strike of the selected fault segments by quantifying the cumulative displacement (CD) and the last displacement increment (LDI) representing the youngest slip event at the selected fault scarps.

The northern tip point of the analyzed fault scarp at the CJS is located at a 280 m long step over, where the total displacement tapers off to zero, while the adjacent subsegment to the north (Figure 2b) shows increasing displacement (Figure 8b). At the southern tip, the displacement tapers off to zero, and the surface expression of the fault dies out. The pattern of displacement distribution is highly variable and does not show a symmetric distribution with maximum displacement at the center of the fault (Figure 8b). Instead, we observed four local maxima suggesting a multiple rupture history with potential linkage of shorter (sub) segments. The maximum measured CD is 8.5 m, with an average of 5.5 m. Sections of the fault scarp with

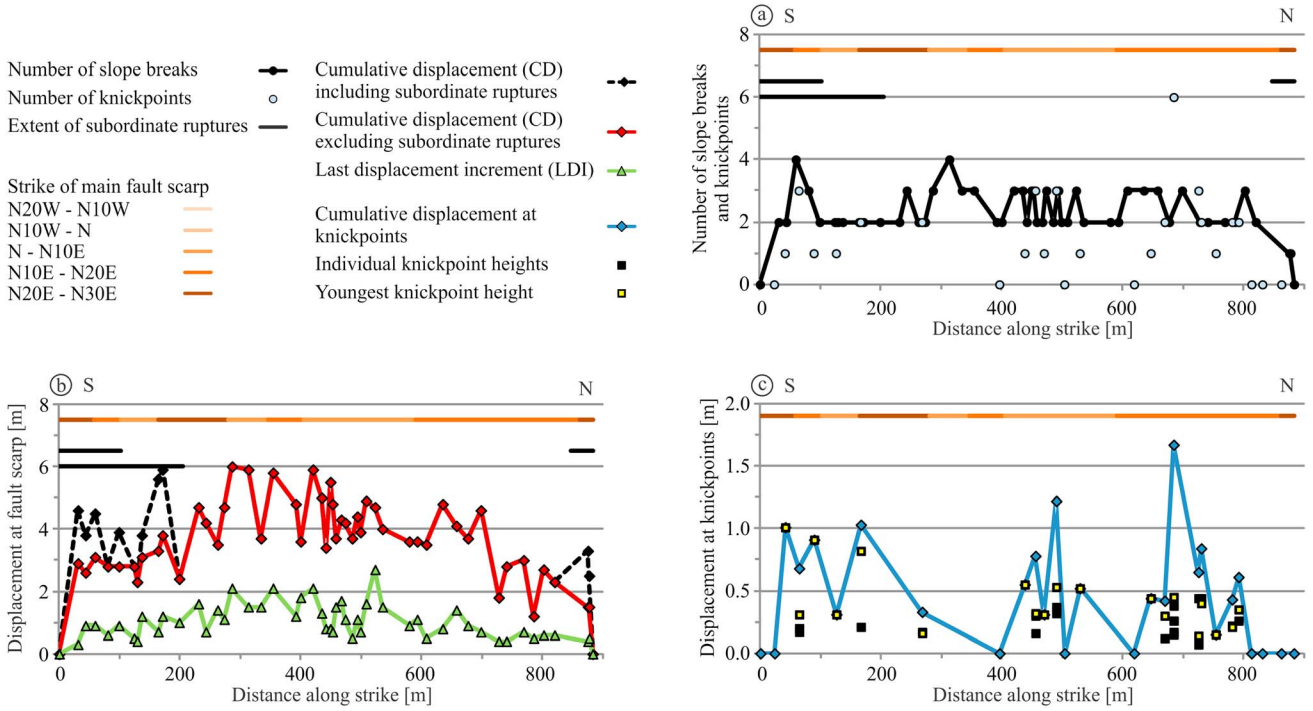

Figure 10. (a) Along-strike distribution of slope breaks and knickpoints in the La Negra segment. The number of slope breaks is two to three with a few exceptions. The number of knickpoints tends to be equal to or one less than the number of slope breaks in the fault scarp. Horizontal lines represent the extent of subordinate ruptures and the strike of the analyzed subsegment. (b) Along-strike displacement distribution. Low CD tends to correlate with the occurrence of subordinate ruptures. The LDI pattern is quite similar to the pattern of CD. (c) Vertical displacement recorded at knickpoints. The solid line shows the cumulative vertical displacement. Black squares show individual knickpoint heights. Light squares mark the most recent knickpoints directly at the fault scarp.

significantly lower than average displacement correlate with the extent of subordinate ruptures (Figure 8b), suggesting that part of the displacement is distributed over several (sub) parallel faults. The LDI along strike of the selected fault scarp is approximately stable ranging between 1.5 and 2.0 m (Figure 8b). The maximum value is 4.7 m and the average is 1.8 m. Near the tips of the rupture, the displacement tapers off to zero. Local maxima partly correlate with maxima in the CD displacement pattern. Comparing the CD and LDI distribution, we observed that the LDI does not resemble the pattern with multiple well-delimited local maxima. This suggests that the displacement was evenly distributed along the rupture during the last surface-breaking event. However, we have to point out the exceptional local maximum near the southern tip of the analyzed rupture, where we could not discriminate multiple events from the geomorphic record.

In general, fault scarps along the LNS are not as well expressed as in the CJS and tend to occur in sets of (sub) parallel scarps extending over broader areas than in the CJS. The fault scarp selected for detailed analysis of displacement distribution is continuous along most of its length (Figure 3b), except near its terminations, where it is characterized by the occurrence of splay faults. The maximum CD along the fault scarp is 6.0 m and, the average is 3.7 m. Lower displacements in the southern and northern portions of the fault scarp correlate with the occurrence of splay faults (Figure 10b). The pattern of displacement is almost symmetric about the center. However, we observe significant differences in CD ranging between the average and the maximum displacement over distances of a few tens of meters. The maximum measured LDI along the fault scarp is 2.7 m with an average of 1.0 m. The displacement pattern of the LDI resembles the pattern of the CD (Figure 10b). Its maximum values are located near the center of the rupture and taper off toward the tips in a symmetric fashion. Graphically, local maxima and minima in the LDI pattern appear to correlate with the CD pattern.

5.4. Knickpoints

The alluvial fans that are offset by the SCF are heavily dissected by numerous small rills, gullies, and wider channels draining the eastern piedmont of the Coastal Cordillera ranges (Figures 2c and 3c). The cross-sectional widths of channels crossing the fault scarp range from a few decimeters to ~10 m (Figure S3 in the supporting

information). The widest channels are associated with large catchment areas of up to 2 km^2, draining the mountain ranges to the west. Smaller gullies and rills have their sources on the inactive fan surfaces of the first generation immediately west of the fault scarp. The drainage system locally displays a complex braided system. Stream orders [*Strahler*, 1957] for channels originating at the abandoned fan surfaces west of the studied surface ruptures range between 1 and 3 and represent narrow gullies with a width of a few decimeters to ~3 m (Figure S3). Channels with stream order of 4 or 5 usually show wider cross-sectional profiles (3–10 m) when crossing the fault scarp. Knickpoints tend to occur in narrow channels with a stream order up to 3, though not every channel with a low stream order developed knickpoints. Conversely, we observed a few knickpoints in channels with stream order > 3. Thus, the stream order may influence the probability of knickpoint preservation but is not a definitive criterion. Channel width and drainage basin size appear to be the most significant factors for knickpoint preservation. Major channels have been observed to lack knickpoints at the analyzed surface ruptures. This may be explained by the high erosive power during episodic rain events [e.g., *Vargas et al*., 2000, 2006].

As aforementioned, the occurrence of knickpoints in the studied section of the CJS is restricted to the main fault scarp and few subordinate ruptures. We identified a total number of 55 knickpoints in a group of 68 selected channels. Fifty of these knickpoints occur within 5 m distance upstream from the surface rupture and have been selected for further analysis. We observed a maximum number of three knickpoints per channel (Figure 8a). The majority of channel profiles with knickpoints comprise only one (20 channels) or two knickpoints (12 channels). Half of the investigated channels (34 channels) do not show knickpoints. The number of knickpoints varies along strike, especially near bends and subordinate ruptures (Figures 7 and 8a). We observed that an increased occurrence of knickpoints in channels coincides with local maxima in the pattern of CD recorded at the fault scarp (Figures 8b and 8c). Sections without any knickpoints correlate with local minima in the CD pattern. The largest gap was observed in the southern portion of the rupture, characterized by a significant change in strike (Figures 7 and 8a). The highest cumulative displacement recorded by knickpoints (1.85 m) occurs in the central section of the rupture. The tallest most recent knickpoint is 1.70 m and is also located in the central portion of the rupture.

Over the LNS we identified a total number of 83 knickpoints in a group of 26 selected channels. Seventy-three of these knickpoints are located within 20 m upstream of the rupture, and 58 occur within 10 m distance. To maintain comparability with the CJS, we selected a subset of 38 knickpoints located within 5 m of the rupture for further analysis. Within the 5 m limit, the maximum number of knickpoints observed in an individual channel was six (Figures 9 and 10a). All other examined channels contained a maximum amount of three knickpoints. The majority of channel profiles show only one (eight channels) or two knickpoints (six channels). Four channel profiles contain three knickpoints. Seven out of 26 examined profiles did not contain any knickpoints within the defined limit. Generally, knickpoints occur along the whole length of the analyzed rupture except near the tips of the rupture. The knickpoint displacement pattern the along strike of the rupture shows three sections, which do not resemble the distribution of CD or LDI recorded by the fault scarp. Local minima of CD at the fault scarp coincide with a lower number or absence of knickpoints (Figure 10c), but we note that the channel profile with six knickpoints is also located in a section of the fault scarp characterized by a very similar CD value. The maximum cumulative displacement recorded by knickpoints is 1.67 m, accounted by six individual knickpoints (Figures 10a and 10c). The highest cumulative displacement resulting from three knickpoints is 1.22 m. The tallest most recent knickpoint in the analyzed portion of the LNS is 1.00 m.

5.5. Estimation of Paleomagnitudes From Surface Rupture Lengths and Displacement Measurements

Surface rupture lengths obtained from fault mapping and vertical displacements derived from the analysis of topographic profiles can be used to approximate paleomagnitudes if single events can be discriminated from the complex rupture history of the selected fault segments. For the determination of paleomagnitudes we applied empirical regression functions formulated by *Wells and Coppersmith* [1994] and *Stirling et al*. [2002]. We calculated and compared paleomagnitudes from (a) the surface rupture length (SRL) using four different regression functions (see Table 1, equations (1)–(4)), (b) the last displacement increment (LDI, equation (5)), and (c) displacements recorded at knickpoints (KnpD) using the same regression function as in (b).

We have mapped 76 individual surface ruptures in the CJS (Figure 2) and 32 in the LNS (Figure 3). We also examined the surface ruptures in the field and on high-resolution aerial data sets [*Bucher et al*., 2012] to determine the longest potential SRL for a single event. For surface ruptures with similar geomorphic

Table 1. Regression Functions for Calculation of Paleomagnitudes

Regressions of Surface Rupture Length (SRL) (km) and Mw		
All slip type; *Wells and Coppersmith* [1994]	$Mw = 5.08 + 1.16*\log(SRL)$	equation (1)
Normal fault slip; *Wells and Coppersmith* [1994]	$Mw = 4.86 + 1.32*\log(SRL)$	equation (2)
Instrumental data; *Stirling et al.* [2002]	$Mw = 5.45 + 0.95*\log(SRL)$	equation (3)
Preinstrumental data; *Stirling et al.* [2002]	$Mw = 5.89 + 0.79*\log(SRL)$	equation (4)
Regression of Displacement (D) (m) and Mw		
Normal fault slip; *Wells and Coppersmith* [1994]	$Mw = 6.61 + 0.71*\log(D)$	equation (5)
Regression of Mw and SRL (km)		
Normal fault slip; *Wells and Coppersmith* [1994]	$\log(SRL) = -2.01 + 0.50*Mw$	equation (6)

characteristics we added up the individual SRL, resulting in a total SRL of 19 km for the CJS and 3.3 km for the LNS, respectively. Based on the 76 individual SLR mapped in the CJS, the paleomagnitudes range from $M_w = 2.9$ to 6.1, depending on the regression function (Figure 11a). We note that the regression functions proposed by *Stirling et al.* [2002] yield significantly higher magnitudes ($M_w = 4.0$ to 6.1) than the ones proposed by *Wells and Coppersmith* [1994] (Table 1, equations (1)–(4)). The maximum potential paleomagnitude for the CJS, based on the total segment length of 19 km, between 23.37°S/70.18°W and 23.53°S/70.25°W, ranges from $M_w = 6.5$ to 6.9. For the LNS, paleomagnitudes based on 32 individual SRL range from $M_w = 2.8$ to 5.9, depending on the regression function (Figure 11b). Using the total length of 3.3 km, we estimated a maximum potential paleomagnitude of $M_w = 5.5$–6.3.

Estimations of paleomagnitudes for the most recent events are based on the LDI values. For the CJS, the resulting paleomagnitudes range from $M_w = 6.6$ to 7.1 (Figure 12a). In the case of the LNS, the resulting paleomagnitudes range from $M_w = 6.3$ to 7.0 (Figure 12b).

Based on the height of 50 selected knickpoints located at the analyzed surface rupture in the CJS (Figure 8c), we calculated paleomagnitudes varying from $M_w = 5.9$ to 6.8 (Figure 12a). For a direct comparison with the paleomagnitudes based on LDI, we also calculated paleomagnitudes using the youngest 34 knickpoints only. These are expected to give the best estimate of the last, potentially seismic displacement, as they represent the least modified subsample of knickpoints. At the CJS, paleomagnitudes for this subsample also range from $M_w = 5.9$ to 6.8, because both the largest and smallest detected knickpoints in our sample were located directly at the fault scarp. For the LNS, the calculated paleomagnitudes based on 38 individual knickpoint heights (Figure 10c) range between $M_w = 5.8$ and 6.7 (Figure 12b). Taking into account only the youngest 19 knickpoints, the results range from $M_w = 6.0$ to 6.6.

6. Discussion

6.1. Quantification of Paleoearthquakes (Slope Breaks Versus Knickpoints)

Multiple slope breaks in the upper part of degraded fault scarps have been reported to represent individual faulting events in the case of, e.g., the Pearce Scarp in Nevada, which has been rejuvenated by the 1915 $M_L = 7.2$

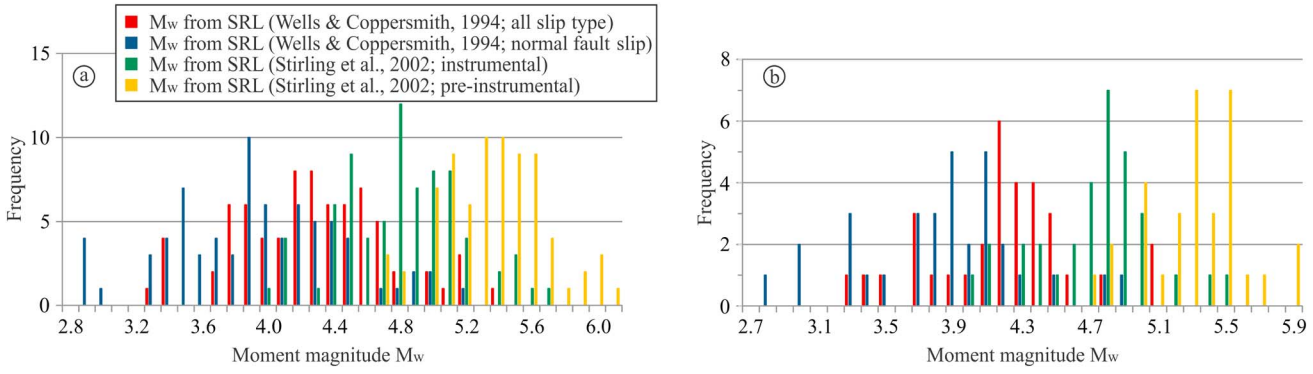

Figure 11. Distribution of paleomagnitudes calculated with regression functions proposed by *Wells and Coppersmith* [1994] and *Stirling et al.* [2002] (Table 1, equations (1)–(4)). (a) Paleomagnitudes based on 76 SRL from the CJS. (b) Paleomagnitudes based on 32 SRL from the LNS. See text for discussion.

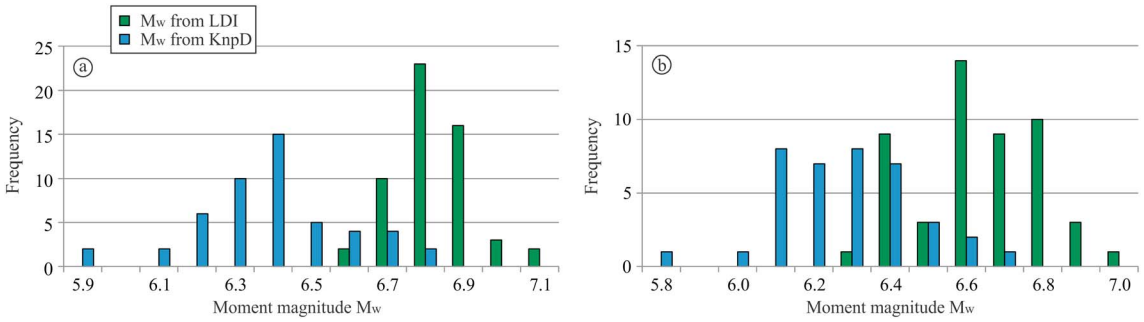

Figure 12. Distribution of paleomagnitudes based on the last displacement increment (LDI) measured at the fault scarp and displacements measured at knickpoints (KnpD). Magnitudes were calculated with a regression function proposed by *Wells and Coppersmith* [1994] (Table 1, equation (5)). (a) CJS. (b) LNS. See text for further discussion.

Pleasant Valley earthquake [*Wallace*, 1984], and the Madison Range Scarp in Montana, which was reactivated in the 1959 $M = 7.1$ Hebgen Lake earthquake [*Wallace*, 1980]. Although it is possible that subtle inflections in slope can be created by small-scale erosional events or multiple step faults resulting from a single event [*Slemmons*, 1957; *McCalpin*, 2009], there are several arguments supporting the occurrence of repeated surface-faulting events at the SCF. First, we observed similar numbers of slope breaks (Figures 7 and 9) along strike of the studied segments except near the tips, where displacement tapers off and the number of slope breaks decreases (Figures 8a and 10a). The occurrence of small-scale erosional events cannot be ruled out, but they are expected to be very localized, and it is unlikely that such events occurred along significant portions of the analyzed surface ruptures. Second, the number of detected slope breaks is well in agreement with the number of colluvial wedges found in the paleoseismological trenches at the studied fault segments [*Robinson et al*., 2011; *Cortés*, 2013]. Therefore, we argue that slope breaks can be used as indicators for the number of surface-rupturing earthquakes.

We also tested the potential of knickpoints as geomorphic markers for the number of paleoearthquakes by determining the number of knickpoints in individual channel profiles and comparing them with (a) the number of events derived from paleoseismological trench logs, and (b) the number of slope breaks along the analyzed fault scarp. Generally, the number of detected knickpoints in both study areas is in quite well agreement with the number of events reported for the SCF in the last 13 ka [*Robinson et al*., 2011; *Cortés*, 2013]. The LNS shows a stronger variation in knickpoint number per channel and a spatially wider distribution of knickpoints than the CJS. If we assume comparable erosion rates for both fault segments, this implies the existence of a suite of knickpoints possibly related to older surface-rupturing events in the LNS. This raises the question if the LNS has experienced more surface-rupturing events than the CJS, which however are not recorded in the slope break record. A possible explanation for the discrepancies between the slope break record and the number of knickpoints might be the potentially older age of the earliest faulting events. According to our sensitivity analysis (see supporting information), for knickpoints with an age exceeding 40 ka, the counterpart in the slope break record may be beyond the maximum resolution of our method.

To further test the agreement between knickpoint record and fault scarp morphology, we compared the number of slope breaks in the fault scarp profiles with the number of knickpoints in adjacent gullies. In a first step, we looked for an exact match between the number of slope breaks in the fault scarp profiles and the number of knickpoints in adjacent channels. For this purpose we selected pairs of scarp and gully profiles separated by an average distance of 18 m (CJS) and 8 m (LNS). In the CJS, we found that only 13 out of 85 profile pairs (15.3%) show an exact match. In the LNS, 12 out of 47 pairs (25.5%) have the same number of slope breaks and knickpoints (Table 2). Note that the total number of tested profiles pairs is higher than the number of acquired gully profiles as in some cases we measured fault scarp profiles directly north and south of a gully allowing for additional profile pairs. Subsequently, we looked for an exact match, but allowed an additional knickpoint. The result was considered positive if the number of slope breaks and knickpoints was equal or if we counted one knickpoint more than the number of slope breaks. For the CJS, the results did not change (Table 2), as there is not a single profile pair where the number of knickpoints is larger than the number of slope breaks in the fault scarp. In case of the LNS, 3 out of 47 profile pairs showed more knickpoints than slope breaks, but in this segment the total number of knickpoints that migrated out of the

Table 2. Correlation Between Number of Slope Breaks and Number of Knickpoints

	Cumbre Jequier Segment		La Negra Segment	
Number of gully profiles		68		26
Number of scarp profiles		59		50
Number of profile pairs		85		47
Number of knickpoints		50		38
Exact match	15.3%	13	25.5%	12
Exact match or 1 knickpoint more	15.3%	13	31.9%	15
Exact match or 1 knickpoint less	**45.9%**[a]	39	**55.3%**[a]	26

[a]Values in bold are the highest percentage of matches.

selected observation window is much higher than in the CJS. In a last test, we allowed the number of knickpoint to be one less than the number of slope breaks. The result was considered positive if the number of slope breaks and knickpoints was equal or if we counted one knickpoint less than the number of slope breaks. In this case, 39 out of 85 profile pairs in the CJS (45.9%) showed a correlation (Table 2). In the LNS, the number of matching pairs increased to 26 out of 47 (55.3%).

These results point to a moderate correlation between the number of surface-rupturing events recorded by slope breaks in fault scarp profiles and the number of knickpoints in the channels, if we allow for a knickpoint less. This initially unexpected result can be explained by taking a close look at the temporal evolution of the fault scarp, shown in the conceptual model of Figure 13. In one possible scenario, starting with an unfaulted block, the first surface-breaking event produces the initial fault scarp (Figure 13, sequence A). After the topography has been put into disequilibrium, channels start to incise into the fault scarp. Later, the first knickpoint is created after channel formation during the second faulting event, while the fault scarp is rejuvenated and subsequently degraded by erosion. This sequence can be repeated multiple times yielding a knickpoint number that equals the number of slope breaks in the fault scarp minus 1. Alternatively, if a channel was present on the fan surface before the first faulting event (Figure 13, sequence B), the number of slope breaks and knickpoints would match exactly for the same sequence of events.

Based on the above results, we find that slope breaks are useful and easily accessible geomorphic markers, which allow to determine the number of surface-rupturing events. Knickpoints, however, seem to be less reliable, probably due to more powerful erosional forcing within the channels. Thus, we conclude that the presented approach should always use both markers or only slope break analysis. Knickpoints alone should not be used as sole indicator for the number of events even in the driest environment.

6.2. Quantification of Vertical Displacement (Slope Breaks Versus Knickpoints)

If the hypothesis that individual knickpoints formed as the result of seismic displacement during consecutive surface-rupturing events is correct, then the height of knickpoints may eventually represent seismic displacement. To test the potential of knickpoints as proxy for potential seismic displacement, we compared knickpoint heights with the displacement recorded by the fault scarp. In a first, crude approach without taking into account any vertical erosion of the knickpoints, we calculated the sum of knickpoint heights within a maximum distance of 5 m upstream and compared the result with the CD recorded at the fault scarp. Subsequently, we compared the height of the most recent knickpoints with the LDI.

In the CJS, we observed an increased number of knickpoints in channels located near to maxima in the CD pattern at the fault scarp (Figures 8b and 8c). The highest cumulative displacement recorded by knickpoints (1.85 m) was observed in the central section of the rupture, where the CD is at the fault scarp is >8 m. This equals ~23% of the CD. Comparing the average CD recorded by the fault scarp (5.5 m) with the average cumulative knickpoint displacement (0.73 m), the percentage of potential seismic displacement recorded by the knickpoints would be 13%. These comparisons give us the lowermost estimate for the percentage of potential cumulative seismic displacement. The location of the tallest most recent knickpoint (1.70 m) coincides with an LDI of 1.70 m, implying that this knickpoint recorded 100% of the seismic displacement of the last surface-breaking event. However, this is an exception. Comparing 47 profile pairs, we found that only two knickpoints may represent the full potentially seismic displacement. For 30 out of 47 profile pairs the most recent knickpoint reflected only up to 30% of the LDI.

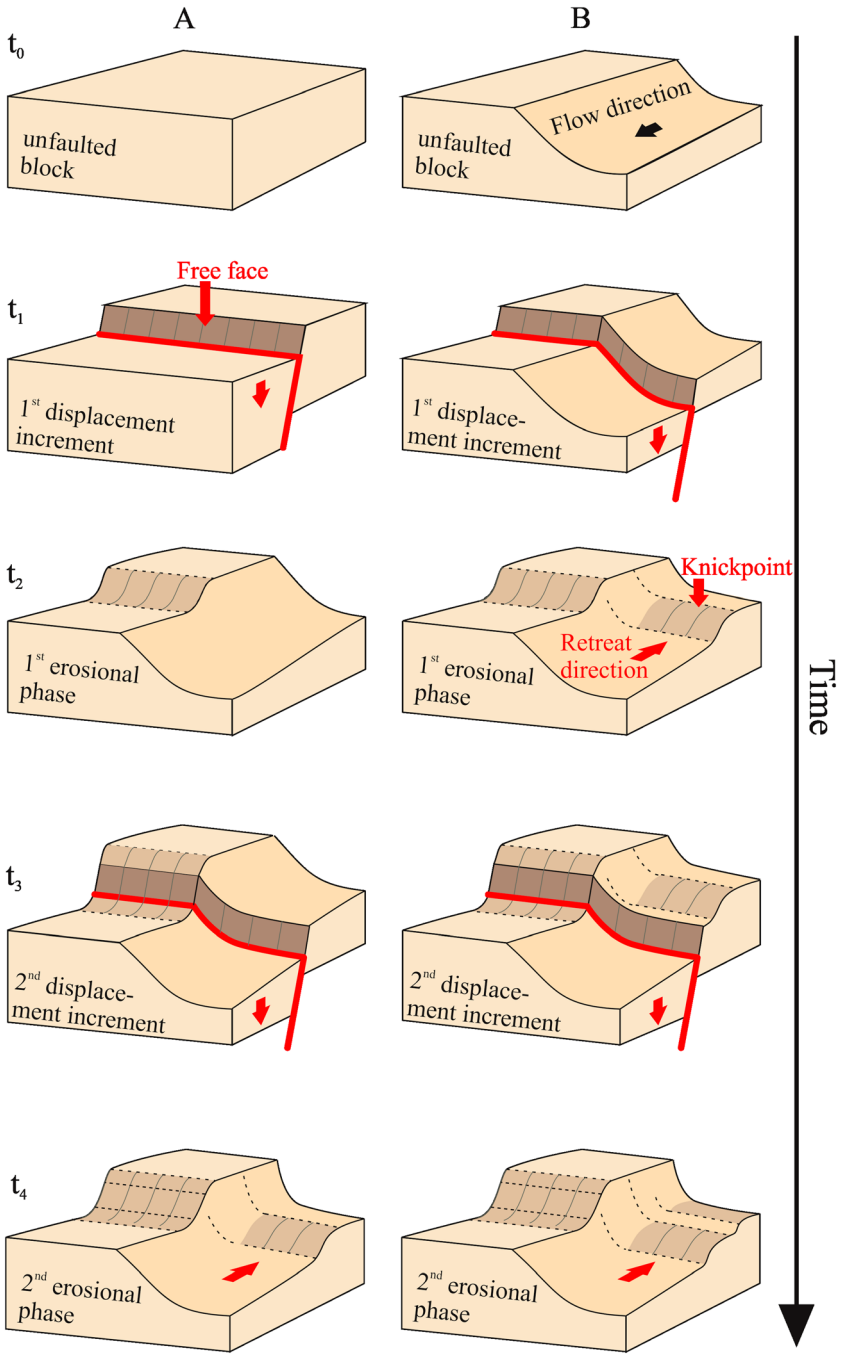

Figure 13. Temporal evolution of a fault scarp. Sequence A shows the evolution over two displacement increments starting with an unfaulted block without channels while Sequence B shows an alternative with a preexistent channel. Starting with an unfaulted block (t_0), the first surface-breaking event produces the initial fault scarp (t_1). After the formation of the fault scarp, channels start or continue to incise, the fault scarp degrades, and potential knickpoints migrate upstream with time (t_2). The subsequent event rejuvenates the fault scarp and produces a first (A) or a second (B) knickpoint (t_3). After the second event erosion degrades the rejuvenated fault scarp, and knickpoints migrate upstream (t_4). Both sequences A and B may be continued for an arbitrary number of events.

Comparing the highest cumulative displacement recorded by knickpoints in the LNS (1.22 m) with the CD of >4 m measured at the adjacent portion of the fault scarp (Figure 10), the lower bound of cumulative seismic displacement would be ~28%. Using the average CD at the fault scarp (3.7 m) and the average cumulative displacement from knickpoint heights (0.68 m), the lowermost estimate of cumulative seismic displacement is

significantly lower (~18%). The tallest most recent knickpoint (1.00 m) does not match the adjacent LDI values of 0.90 and 0.30 m. Comparing 35 profile pairs, we found that in 18 out of 35 cases, the knickpoints may have retained up to 50% of the LDI. Only four out of 35 knickpoints seem representative of the full seismic displacement.

Along both studied fault segments, we observed channels with a high cumulative displacement at knickpoints in spite of a below average CD at the fault scarp pointing to a complex rupture history. Comparing the displacement recorded by the most recent knickpoints to the LDI value derived from adjacent scarp profiles, we note that there are only a few knickpoints, which have retained the full seismic displacement. The majority of knickpoints appear to have suffered from vertical erosion and have only retained a fraction of the LDI. A better record of the most recent displacement is found by analyzing the steepest part of the fault scarp, the LDI. This may be explained by differences in erosion processes and rates. While we expect a uniform erosion of the fault scarp, the erosional processes and stresses in channels may differ significantly depending on, e.g., drainage area or channel width. We conclude that the knickpoint record may complement the information derived from fault scarp analysis, but is highly variable depending on, e.g., channel width or drainage area.

6.3. Segmentation, Fault Growth Models, and Displacement Variability

The careful examination of displacement patterns along strike can provide important information on the fault evolution at different points in time and help to detect possible changes in behavior. The along-strike displacement patterns show maximum CD near the center and decreasing displacement toward the tip points (Figures 8b and 10b). However, CD varies strongly over short distances. This is potentially related to the occurrence of subordinate ruptures and changes in strike direction. In the CJS, the LDI tends to be more stable than the CD (Figure 8b), suggesting a uniform displacement distribution along strike in the last surface-breaking event. In the LNS, the LDI pattern resembles the CD pattern (Figure 10b), although with significantly smaller variations possibly suggesting the existence of incremental displacement variability along strike between individual events. The extraction of the penultimate or even antepenultimate displacement increment could provide a more detailed picture of the fault evolution. However, this record is expected to be biased due to erosion and could only provide minimum estimates.

Comparing both the maximum and the average CD values in both study areas, the LNS is clearly characterized by a lower CD than the CJS. This can be attributed to the distribution of displacement over a larger number of subordinate ruptures and splay faults. Comparing the LDI values, the LNS is again characterized by lower displacements. This suggests that the most recent events on the two fault segments may have been individual surface-breaking events of different size. Another possible explanation is that the LNS, which is located near the southern termination of the SCF (Figure 1b), experienced less displacement in the most recent large earthquake than the CJS. Another factor to consider is the strike direction of the segments. The average strike at CJS is N25°E, while the LNS strikes N12°E. Depending on the stress field, the CJS may be in a more favorable orientation for reactivation. The strike direction of the fault segment may also influence rupture propagation. We have observed changes in the number of events preserved in the geomorphic record near bends within the analyzed segments, especially along the CJS (Figures 7 and 8). Irregularities in the fault geometry, such as bends or overlaps, may even stop rupture propagation [e.g., *Sibson*, 1989].

The comparison of mapped SRL and measured vertical displacements raises further questions concerning the segmentation of the SCF and the interplay of segments during large earthquakes. CD and LDI values along the studied segments appear too high compared to individual SRL. In addition, we observed that the CD stays stable at step overs if we take into account the displacement recorded by overlapping, adjacent ruptures (Figure 8b). This suggests a joint rupture of multiple (sub) segments during large earthquakes. We also calculated synthetic SRL from paleomagnitudes, which were previously determined based on measured vertical displacements (Table 1, equation (6); see supporting information). Comparing these to mapped SRL, we found that individual SRL in the studied segments are significantly shorter, again suggesting that large earthquakes involve multiple (sub) segments. Another possible explanation for the discrepancy between measured displacements and individual SRL is the occurrence of earthquake clusters with significantly lower magnitudes activating individual fault segments on a very short timescale of minutes, days, or weeks. *Caskey and Wesnousky* [1997] and *Caskey et al*. [2004] reported a similar behavior for the 1954 Fairview Peak and Dixie Valley earthquakes, which produced a zone of surface ruptures extending for 100 km. Such consecutive surface-breaking events cannot be discriminated with the proposed methods.

Below we discuss the most likely fault growth scenarios. In both fault segments the number of surface-rupturing events in the geomorphic record is higher in the center than toward its tips. The CD patterns show displacement maxima at or near the center. This suggests that the fault segments grew from the center toward the tips over the slip history of the structure. The LDI values along the studied segments appear to be too high compared to the mapped individual SRL. This points to a mode of fault growth where the vertical displacement increases faster than the fault length. A constant length growth model was proposed by *Walsh et al.* [2002]. At a larger scale, the investigated segments are likely to have developed by linkage of individual ruptures as suggested by the model of *Peacock and Sanderson* [1991], which is supported by the observation of numerous step overs along the studied fault segments.

Overall, the vertical displacements (CD, LDI, and KnpD) and the SRL suggest a complex behavior of the studied fault segments. Spatial and temporal displacement variability has been reported for numerous faults, e.g., the Rangitaiki Fault in New Zealand [*Bull et al.*, 2006], particularly for short time intervals of a few ka. The authors link the displacement variability to segment interaction and suggest that individual surface-rupturing events may be confined to specific fault segments. A similar example of displacement variability has been reported by *Peacock and Sanderson* [1991] for the Kilve fault zone in the Bristol Channel Basin and again linked to the interplay of individual fault segments. Further examples have been reported by, e.g., *Caskey et al.* [2004] and *Densmore et al.* [2007], showing that faulting is indeed highly variable, particularly when investigated on relatively short timescales encompassing only few surface-rupturing events.

6.4. Approximation of Paleomagnitudes

To improve the significance of topographically derived surface displacements and rupture lengths for the approximation of paleomagnitudes, we calculated potential magnitudes based on three different values measured along strike of the studied fault segments. We compare the results of our calculations (Figures 14 and 15; Table 3) with paleomagnitudes derived from the analysis of colluvial wedges present in the paleoseismological trenches at the SCF [*Cortés*, 2013].

We note that the paleomagnitudes derived from the total SRL of the CJS ($M_w = 6.5$ to 6.9) are well in agreement with the paleomagnitudes calculated from LDI ($M_w = 6.6$ to 7.1, Figure 14). The maximum paleomagnitudes derived with this approach also compare well with a maximum paleomagnitude of $M_w \sim 7$ determined by trench log analyses [*González et al.*, 2010; *Cortés*, 2013], and thus, are considered to be the most reliable estimates. Paleomagnitudes derived from KnpD ($M_w = 5.9$ to 6.8) yield minimum estimates. Along the LNS, paleomagnitudes based on LDI ($M_w = 6.3$ to 7.0) and on displacement recorded by the youngest knickpoints ($M_w = 6.0$ to 6.6) show the best agreement (Figure 15), and agree with the paleoseismological results as well. The paleomagnitudes based on total SRL of the LNS ($M_w = 5.5$ to 6.3) are significantly lower.

The wide range of results highlights the uncertainties of the method. Not only it is difficult to define rupture endpoints from paleoruptures, but it is also clear that even if the SLR is well known it yields a wide span of results depending of the regression method applied for calculation of paleomagnitudes (Tables 1 and 3). A limit for the determination of the end of an individual rupture has been proposed by *Wesnousky* [2006] who observed that earthquake ruptures tend to stop at geometrical irregularities. Major gaps of 3–4 km in the fault trace are likely to stop the rupture process. At discontinuities of <3 km, the observations indicate that ruptures cease propagation in approximately 40% of the time. Based on our field investigations we can determine the ends of rupture propagation at least for the past three events along the two investigated segments, yet the gaps between adjacent segments are significantly shorter (≤ 2.3 km) than those proposed by *Wesnousky* [2006]. In this scenario we assume that all subsegments ruptured in a single event. A second end-member scenario that can be considered is that each subsegment rupture broke the surface in a single event, which is unlikely, but cannot be entirely excluded as has been shown for earthquake sequences such as the 1954 Dixie Valley earthquake sequence [*Caskey and Wesnousky*, 1997; *Caskey et al.*, 2004]. Further uncertainties—though minor—arise from the standard errors of the regression coefficients [*Wells and Coppersmith*, 1994; *Stirling et al.*, 2002].

Our results suggest that a reliable estimate of paleomagnitudes is possible based on careful mapping of SRL and measurement of vertical displacements recorded at the fault scarp and knickpoints. However, we have to stress the importance of using a combination of various morphological markers for the determination of

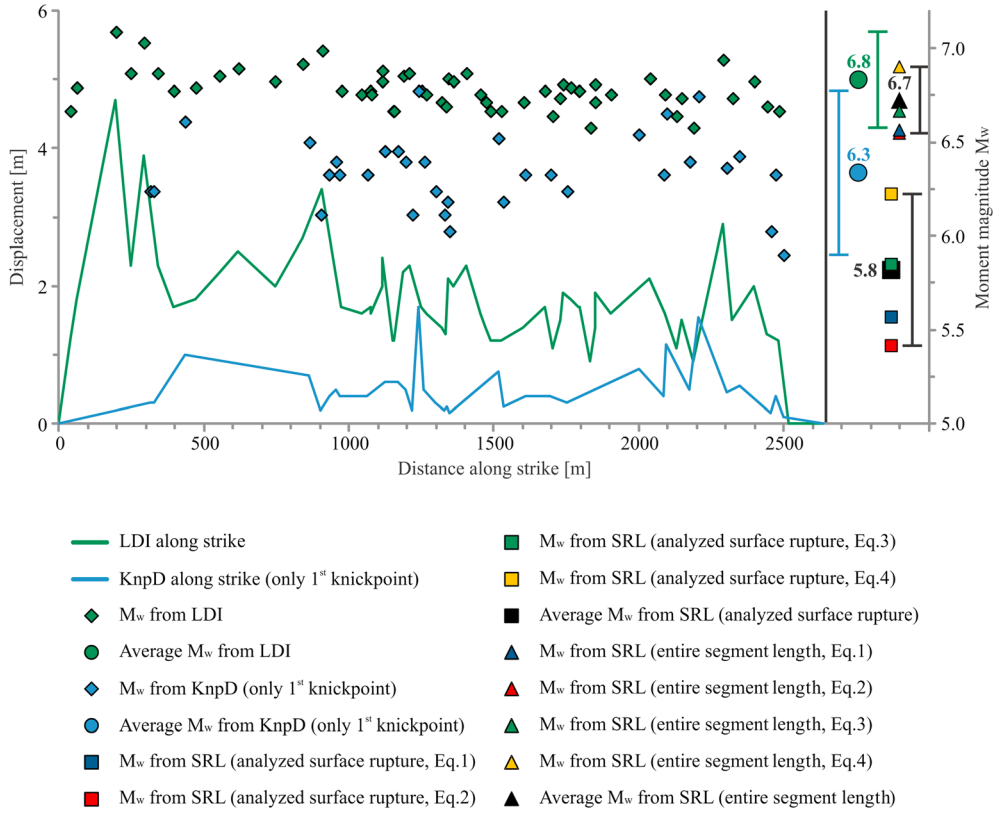

Figure 14. Along-strike distribution of displacement and calculated paleomagnitudes in the Cumbre Jequier segment. Diamonds mark paleomagnitudes calculated from individual displacements. Circles denote average paleomagnitudes. Squares and triangles represent paleomagnitudes calculated from SRL using different regression function proposed by *Wells and Coppersmith* [1994] and *Stirling et al.* [2002]. See text for discussion.

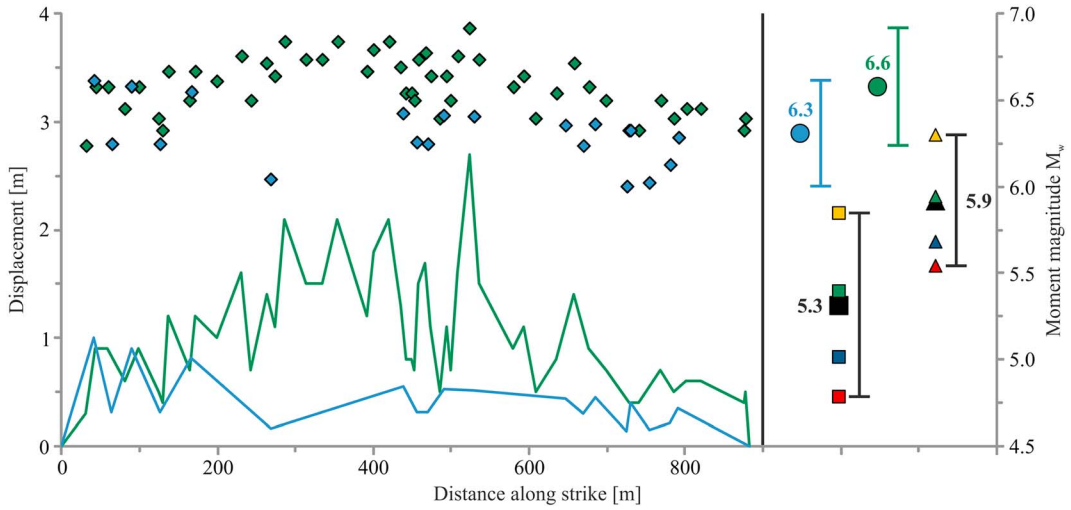

Figure 15. Along-strike distribution of displacement and calculated paleomagnitudes in the La Negra segment. Diamonds mark paleomagnitudes calculated from individual displacements. Circles denote average paleomagnitudes. Squares and triangles represent paleomagnitudes calculated from SRL using different regression function proposed by *Wells and Coppersmith* [1994] and *Stirling et al.* [2002]. See Figure 14 for legend and text for further discussion.

Table 3. Estimation of Paleomagnitudes From SRL, LDI, and KnpD Based on Regression Functions Proposed by *Wells and Coppersmith* [1994] and *Stirling et al.* [2002][a]

	Cumbre Jequier Segment		La Negra Segment	
Input Parameter	Moment Magnitude Range	Number of Input Values	Moment Magnitude Range	Number of Input Values
Individual SRL	2.9–6.1	76	2.8–5.9	32
Total SRL	**6.5–6.9**	1	5.5-6.3	1
LDI	**6.6–7.1**	56	**6.3–7.0**	50
KnpD (all knickpoints)	5.9–6.8	50	5.8–6.7	38
KnpD (only youngest knickpoints)	5.9–6.8	34	**6.0–6.6**	19

[a]Bold values denote the best approximation.

potential paleomagnitudes to avoid overestimations or underestimations, especially in cases of faults with a multiple rupture history and/or a pronounced segmentation. For the analyzed fault segments of the SCF, we find that the combination of total segment length, the last displacement increment, and displacements recorded by the youngest knickpoints yields reliable estimates of paleomagnitude.

6.5. Major Contributions of Our Study

Which sets of information can be retrieved from our study of geomorphic makers? We can distinguish the number of events over large distances of prehistoric fault ruptures to characterize the occurrence and paleomagnitudes of surface-breaking events. In combination with a few trenches to correlate the findings, we can retrieve age constraints allowing to calculate recurrence rates. We can also constrain fault growth patterns along strike and determine segment boundaries for rupture propagation more reliably than from field mapping alone. In addition, our method serves as a guide to determine optimal locations for trenching excavations, based on a strong background of knowledge about the potential number of surface-breaking events, thus avoiding overrepresentation or underrepresentation of paleoearthquakes. This combined approach leads to a more comprehensive understanding of the evolution of the total fault system. Our approach relies on the preservation of subtle morphological structures, and thus, is best suited for studies in arid to hyperarid regions with low erosion rates. Based on the results of the sensitivity tests described in the supporting information, we can detect individual displacement increments over tens of thousands of years in a hyperarid environment. Variations in initial scarp height, maximum scarp slope θ, or background slope α do not have a significant impact on the detection of morphological signals. However, the diffusion constant κ does strongly influence the time window in which our approach yields reliable results, and thus, has to be carefully evaluated. We suggest to conduct similar sensitivity tests to estimate the compatible time window for differing climatic environments. We also note that the forward modeling function used to model the degradation of synthetic elevation profiles may not be suitable for all environments [*Hanks et al.*, 1984; *Hanks and Andrews*, 1989].

Our analysis of geomorphic markers can be combined with findings from paleoseismological trenching to reveal the history of the analyzed faults. In addition to the detailed but very localized information from paleoseismological trench logs, the combined approach of the above described methods allows us to quantify the distribution and variability of surface-breaking events, and thus to investigate fault segmentation and evolution over larger distances along strike leading to a better understanding and assessment of potential seismic hazard.

7. Conclusions

The presented study aimed at testing the applicability of two geomorphic markers, slope breaks, and knickpoints in order to (a) discriminate and quantify individual surface-breaking events along the strike of two selected fault segments of the Salar del Carmen Fault in northern Chile, (b) extract cumulative and incremental vertical displacements from topographic data and investigate the displacement pattern along strike, (c) derive information on fault growth patterns and segmentation, and (d) deduce reliable estimates of paleomagnitudes.

Our approach enables us to detect subtle gradient changes in high-resolution topographic profiles representing individual, potentially seismogenic surface-breaking events at the analyzed fault segments. The presented

method is a well-suited approach to assess the multiple rupture history of a complex fault system and is applicable to all types of fault scarps including composite and multiple scarps.

Comparing our results to findings from paleoseismological trenching campaigns we showed that slope breaks in the fault scarp morphology can be used to quantify the number of surface-breaking events at the studied fault segments. We have to note that the knickpoint record seems to suffer more from erosion, most probably due to larger erosional forcing in the channels. Hence, results of similar analyses using these geomorphic features have to be treated with caution. We conclude that knickpoints are not suitable as a sole quantitative marker for multiple rupture events. In absence of quantitative fault scarp analysis, knickpoints may be used as a qualitative indicator of recent fault rupture.

The vertical displacement patterns along the strike of the studied segments indicate a complex and highly variable history of the faulting process. On the scale of an individual subsegment, the observed displacement patterns suggest fault growth from the center toward the tips. At a larger scale, the investigated segments are likely to have developed by linkage of individual ruptures.

Based on detailed measurements of surface rupture lengths, the most recent vertical displacement increment, and vertical displacements recorded by knickpoints, we were able to estimate paleomagnitudes of potentially seismogenic ruptures at the studied segments which are consistent with paleoseismological trench log analyses. The most reliable estimate can be derived from the last displacement increment in combination with total segment length. Paleomagnitudes derived from displacements recorded by knickpoints are considered a minimum estimate due to vertical erosion during retreat.

The main added values of our approach to sole paleoseismological trenching are (a) the use of various independent parameters measured directly at the surface rupture instead of secondary evidence as, e.g., the thickness of colluvial wedges, which may be modified by rupture complexities, (b) the number of events and the displacement pattern can be investigated over large distances along the fault, and (c) this approach can be used in remote, hardly accessible areas if high-resolution topographic data sets are available. Our methods may facilitate the finding of appropriate locations for paleoseismological trenching. In combination with a few trenches to correlate the findings, age constraints can be retrieved and used to calculate recurrence rates. This combination of geomorphological and paleoseismological techniques may lead to a better understanding of complex and transient faulting processes.

Data and Resources

Topographic profiles used for analysis have been acquired with Differential GPS during several field campaigns. The data as well as the Matlab codes used for analysis can be provided on request.

1. Figure 1 uses background images created from the ASTER Global Digital Elevation Map V1 available at http://asterweb.jpl.nasa.gov/gdem.asp (retrieved: 7 July 2010).
2. Figures 2 and 7 use background imagery from Google Earth.
3. Figures 2, 3, 7, 9, S1, and S2 use background images created from high-resolution topographic and visual data set acquired with the Modular Airborne Camera System, developed by the DLR (German Aerospace Center) [*Lehmann et al*., 2011; *Bucher et al*., 2012]. Contact address for data requests: Pia Victor (Department of Geodynamics, GeoForschungsZentrum Potsdam, Telegrafenberg, D-14473 Potsdam, Germany. E-mail: pvictor@gfz-potsdam.de).

Acknowledgments
This research (project VI 497/2-1) has been funded by Deutsche Forschungsgemeinschaft (DFG) within scope of the DFG bundle PAK 464. Additional funding for field work has been provided by GFZ Potsdam. We wish to thank Gabriel González (Universidad Católica del Norte, Antofagasta, Chile) for support during field campaigns and interesting discussions. We also thank Olaf Zielke (King Abdullah University of Science and Technology, Thuwal, Saudi Arabia) for interesting discussions on fault scarp evolution, and Manuela Dziggel (GFZ Potsdam) for help with figure design. Additional thanks go out to Tilman Bucher and Jörg Brauchle (German Aerospace Center DLR). Finally, we thank the Editors and the reviewers Steve DeLong and Felipe Aron for their numerous constructive comments, which helped to improve the manuscript.

References

Allmendinger, R. W., and G. González (2010), Invited review paper: Neogene to Quaternary tectonics of the coastal Cordillera, northern Chile, *Tectonophysics*, *495*(1–2), 93–110.

Andrews, D. J., and T. C. Hanks (1985), Scarp degraded by linear diffusion: Inverse solution for age, *J. Geophys. Res.*, *90*(B12), 10,193–10,208, doi:10.1029/JB090iB12p10193.

Armijo, R., and R. Thiele (1990), Active faulting in northern Chile: Ramp stacking and lateral decoupling along a subduction plate boundary?, *Earth Planet. Sci. Lett.*, *98*(1), 40–61.

Avouac, J.-P., and G. Peltzer (1993), Active tectonics in southern Xinjiang, China: Analysis of terrace riser and normal fault scarp degradation along the Hotan-Qira Fault System, *J. Geophys. Res.*, *98*(B12), 21,773–21,807, doi:10.1029/93JB02172.

Begin, Z. E. B., D. F. Meyer, and S. A. Schumm (1981), Development of longitudinal profiles of alluvial channels in response to base-level lowering, *Earth Surf. Processes Landforms*, *6*(1), 49–68.

Berlin, M. M., and R. S. Anderson (2007), Modeling of knickpoint retreat on the Roan Plateau, western Colorado, *J. Geophys. Res.*, *112*, F03S06, doi:10.1029/2006JF000553.

Brown, M., F. Diaz, and J. Grocott (1993), Displacement history of the Atacama Fault System 25°00'S-27°00'S, northern Chile, *Geol. Soc. Am. Bull.*, *105*(9), 1165–1174.
Bucher, T., O. Zielke, P. Victor, F. Lehmann, and O. Oncken (2012), Very high resolution photogrammetric DSMs and true-orthoimages: 3D-fault zone mapping in Northern Chile, GeoHannover2012, Hannover, 1–3 Oct.
Bucknam, R. C., and R. E. Anderson (1979), Estimation of fault-scarp ages from a scarp-height–slope-angle relationship, *Geology*, *7*(1), 11–14.
Bull, J. M., P. M. Barnes, G. Lamarche, D. J. Sanderson, P. A. Cowie, S. K. Taylor, and J. K. Dix (2006), High-resolution record of displacement accumulation on an active normal fault: Implications for models of slip accumulation during repeated earthquakes, *J. Struct. Geol.*, *28*(7), 1146–1166.
Buske, S., S. Lüth, H. Meyer, R. Patzig, C. Reichert, S. Shapiro, P. Wigger, and M. Yoon (2002), Broad depth range seismic imaging of the subducted Nazca Slab, North Chile, *Tectonophysics*, *350*(4), 273–282.
Cartwright, J. A., B. D. Trudgill, and C. S. Mansfield (1995), Fault growth by segment linkage: An explanation for scatter in maximum displacement and trace length data from the Canyonlands Grabens of SE Utah, *J. Struct. Geol.*, *17*(9), 1319–1326.
Caskey, S. J., and S. G. Wesnousky (1997), Static stress changes and earthquake triggering during the 1954 Fairview Peak and Dixie Valley earthquakes, central Nevada, *Bull. Seismol. Soc. Am.*, *87*(3), 521–527.
Caskey, S. J., J. W. Bell, A. R. Ramelli, and S. G. Wesnousky (2004), Historic surface faulting and paleoseismicity in the area of the 1954 rainbow mountain-stillwater earthquake sequence, central Nevada, *Bull. Seismol. Soc. Am.*, *94*(4), 1255–1275.
Cembrano, J., G. González, G. Arancibia, I. Ahumada, V. Olivares, and V. Herrera (2005), Fault zone development and strain partitioning in an extensional strike-slip duplex: A case study from the Mesozoic Atacama fault system, Northern Chile, *Tectonophysics*, *400*(1–4), 105–125.
Cortés, J. (2013), Activité des failles de la plaque supérieure dans l'avant-arc côtier du nord du Chili (~23°30'S): Paléosismologie, implications néotectoniques et relation avec le cycle de subduction, PhD thesis, Univ. Toulouse 3 Paul Sabatier, Toulouse, France.
Cortés, J., G. L. González, S. A. Binnie, R. Robinson, S. P. H. T. Freeman, and G. Vargas (2012), Paleoseismology of the Mejillones Fault, northern Chile: Insights from cosmogenic ^{10}Be and optically stimulated luminescence determinations, *Tectonics*, *31*, TC2017, doi: 10.1029/2011TC002877.
Crosby, B. T., and K. X. Whipple (2006), Knickpoint initiation and distribution within fluvial networks: 236 waterfalls in the Waipaoa River, North Island, New Zealand, *Geomorphology*, *82*(1–2), 16-38.
Delouis, B., A. Cisternas, L. Dorbath, L. Rivera, and E. Kausel (1996), The Andean subduction zone between 22 and 25°S (northern Chile): Precise geometry and state of stress, *Tectonophysics*, *259*(1–3), 81–100.
Delouis, B., H. Philip, L. Dorbath, and A. Cisternas (1998), Recent crustal deformation in the Antofagasta region (northern Chile) and the subduction process, *Geophys. J. Int.*, *132*(2), 302–338.
Densmore, A. L., S. Gupta, P. A. Allen, and N. H. Dawers (2007), Transient landscapes at fault tips, *J. Geophys. Res.*, *112*, F03S08, doi:10.1029/2006JF000560.
D'Errico, J. (2007), Movingslope, MATLAB Central File Exchange, retrieved July 24, 2012. [Available at http://www.mathworks.com/matlabcentral/fileexchange/16997-movingslope.]
Dunai, T. J., G. A. G. López, and J. Juez-Larré (2005), Oligocene-Miocene age of aridity in the Atacama Desert revealed by exposure dating of erosion-sensitive landforms, *Geology*, *33*(4), 321–324.
Espinoza, S. R. (1983), Geologia y Genesis de la Mineralizacion Cuprifera del sector Caleta Coloso, al sur de Antofagasta, *Andean Geol.*, 19–20, doi:10.5027/andgeoV10n2-3-a05.
Fu, B., Y. Ninomiya, X. Lei, S. Toda, and Y. Awata (2004), Mapping active fault associated with the 2003 M_w 6.6, Bam (SE Iran) earthquake with ASTER 3D images, *Remote Sens. Environ.*, *92*(2), 153–157.
Gardner, T. W. (1983), Experimental study of knickpoint and longitudinal profile evolution in cohesive, homogeneous material, *Geol. Soc. Am. Bull.*, *94*(5), 664–672.
Gilbert, G. K. (1895), *Niagara Falls and Their History*, *Natl. Geogr. Monogr.*, pp. 203–236, Am. Book Co., New York.
González, G., and D. Carrizo (2003), Segmentación, cinemática y cronología relativa de la deformación tardía de la Falla Salar del Carmen, Sistema de Fallas de Atacama, (23°40'S), norte de Chile, *Rev. Geol. Chile*, *30*(2), 223–244.
González, G., J. Cembrano, D. Carrizo, A. Macci, and H. Schneider (2003), The link between forearc tectonics and Pliocene-Quaternary deformation of the Coastal Cordillera, northern Chile, *J. South Am. Earth Sci.*, *16*(5), 321–342.
González, G., T. Dunai, D. Carrizo, and R. Allmendinger (2006), Young displacements on the Atacama Fault System, northern Chile from field observations and cosmogenic ^{21}Ne concentrations, *Tectonics*, *25*, TC3006, doi: 10.1029/2005TC001846.
González, G., J. Cortés, S. Binnie, R. A. Robinson, and C. Toledo (2010), Paleoseismology of upper plate faults in the Chilean convergent margin: Insights from ^{10}Be and OSL dating, Abstract T33B-2221 presented at 2010 Fall Meeting, AGU, San Francisco, Calif., 13–17 Dec.
Hanks, T. C., and D. J. Andrews (1989), Effect of far-field slope on morphologic dating of scarplike landforms, *J. Geophys. Res.*, *94*(B1), 565–573, doi:10.1029/JB094iB01p00565.
Hanks, T. C., R. C. Bucknam, K. R. Lajoie, and R. E. Wallace (1984), Modification of wave-cut and faulting-controlled landforms, *J. Geophys. Res.*, *89*(B7), 5771–5790, doi:10.1029/JB089iB07p05771.
Hartley, A. J., and G. Chong (2002), Late Pliocene age for the Atacama Desert: Implications for the desertification of western South America, *Geology*, *30*(1), 43–46.
Hartley, A. J., A. E. Mather, E. Jolley, and P. Turner (2005), Climatic controls on alluvial-fan activity, Coastal Cordillera, northern Chile, *Geol. Soc. London Spec. Publ.*, *251*(1), 95–116.
Hassan, M. A., and M. Klein (2002), Fluvial adjustment of the Lower Jordan River to a drop in the Dead Sea level, *Geomorphology*, *45*(1–2), 21–33.
Hervé, M. (1987a), Movimiento sinistral en el Cretácico inferior de la Zona de Falla de Atacama al norte de Paposo (24 S), Chile, *Rev. Geol. Chile*, *31*, 37–42.
Hervé, M. (1987b), Movimiento normal de la falla Paposo, zona de Falla Atacama, en el Mioceno, Chile, *Rev. Geol. Chile*, *31*, 31–36.
Hilley, G. E., and J. R. Arrowsmith (2003), Scarp dater software: Scarp diffusion exercise from the International Quality Network Workshop: Potsdam, Germany, Potsdam Univ.
Holland, W. N., and G. Pickup (1976), Flume study of knickpoint development in stratified sediment, *Geol. Soc. Am. Bull.*, *87*(1), 76–82.
Huang, M.-W., Y.-W. Pan, and J.-J. Liao (2013), A case of rapid rock riverbed incision in a coseismic uplift reach and its implications, *Geomorphology*, *184*, 98–110.
Kaneda, H., et al. (2008), Surface rupture of the 2005 Kashmir, Pakistan, earthquake and its active tectonic implications, *Bull. Seismol. Soc. Am.*, *98*(2), 521–557, doi:10.1785/0120070073.
Kober, F. (2005), Quantitative analysis of the topographic evolution of the Andes of Northern Chile using cosmogenic nuclides, PhD thesis, Swiss Federal Inst. of Technol., Zürich, Switzerland.
Kumar, S., S. G. Wesnousky, T. K. Rockwell, R. W. Briggs, V. C. Thakur, and R. Jayangondaperumal (2006), Paleoseismic evidence of great surface rupture earthquakes along the Indian Himalaya, *J. Geophys. Res.*, *111*, B03304, doi: 10.1029/2004JB003309.

Lehmann, F., R. Berger, J. Brauchle, D. Hein, H. Meissner, S. Pless, B. Strackenbrock, and A. Wieden (2011), MACS—Modular Airborne Camera System for generating photogrammetric high-resolution products, *Photogrammetrie - Fernerkundung - Geoinformation*, *2011*(6), 435–446.
Litchfield, N. J., J. K. Campbell, and A. Nicol (2003), Recognition of active reverse faults and folds in North Canterbury, New Zealand, using structural mapping and geomorphic analysis, *N. Z. J. Geol. Geophys.*, *46*(4), 563–579.
Liu-Zeng, J., et al. (2009), Co-seismic ruptures of the 12 May 2008, Ms 8.0, Wenchuan earthquake, Sichuan: East–west crustal shortening on oblique, parallel thrusts along the eastern edge of Tibet, *Earth Planet. Sci. Lett.*, *286*(3–4), 355–370.
Loveless, J. (2007), Extensional tectonics in a convergent margin setting: Deformation of the northern Chilean forearc, PhD thesis, Cornell Univ., Ithaca, New York.
Loveless, J. P., G. D. Hoke, R. W. Allmendinger, G. González, B. L. Isacks, and D. A. Carrizo (2005), Pervasive cracking of the northern Chilean Coastal Cordillera: New evidence for forearc extension, *Geology*, *33*(12), 973–976.
Loveless, J. P., R. W. Allmendinger, M. E. Pritchard, J. L. Garroway, and G. Gonzalez (2009), Surface cracks record long-term seismic segmentation of the Andean margin, *Geology*, *37*(1), 23–26.
Madugo, C. M., J. F. Dolan, and R. D. Hartleb (2012), New paleoearthquake ages from the Western Garlock Fault: Implications for regional earthquake occurrence in Southern California, *Bull. Seismol. Soc. Am.*, *102*(6), 2282–2299.
Mattson, A., and L. R. Bruhn (2001), Fault slip rates and initiation age based on diffusion equation modeling: Wasatch Fault Zone and Eastern Great Basin, *J. Geophys. Res.*, *106*(B7), 13,739–13,750, doi:10.1029/2001JB900003.
Mayer, L. (1984), Dating Quaternary fault scarps formed in alluvium using morphologic parameters, *Quat. Res.*, *22*(3), 300–313.
McCalpin, J. P. (2009), Paleoseismology, in *International Geophysics*, 2nd ed., vol. 95, 613 pp., Academic Press, Burlington, Mass.
Miller, J. R. (1991), The influence of bedrock geology on knickpoint development and channel-bed degradation along downcutting streams in south-central Indiana, *J. Geol.*, *99*, 591–605.
Naranjo, J. (1987), Interpretación de la actividad cenozoica superior a lo largo de la zona de Falla Atacama, norte de Chile, *Rev. Geol. Chile*, *31*, 43–55.
Naranjo, J., F. Hervé, X. Prieto, and F. Munizaga (1984), Actividad cretácica de la Falla de Atacama al este de Chañaral: Milonitización y plutonismo, *Comunicaciones*, *34*, 57–66.
Nash, D. B. (1980), Morphologic dating of degraded normal fault scarps, *J. Geol.*, *88*(3), 353–360.
Norabuena, E. O., T. H. Dixon, S. Stein, and C. G. A. Harrison (1999), Decelerating Nazca-South America and Nazca-Pacific Plate motions, *Geophys. Res. Lett.*, *26*(22), 3405–3408, doi:10.1029/1999GL005394.
Peacock, D. C. P., and D. J. Sanderson (1991), Displacements, segment linkage and relay ramps in normal fault zones, *J. Struct. Geol.*, *13*(6), 721–733.
Penck, W. (1924), Die morphologische Analyse, Ein Kapitel der physikalischen Geologie, Verlag von J. Engelhorns Nachf., Stuttgart, Germany.
Reutter, K. J., et al. (1994), Geological Map of the Central Andes between 20°S and 26°S (Geology compiled and partly modified by: K.-J. Reutter, R. Döbel, T. Bogdanic, J. Kley), in *Tectonics of the Southern Central Andes*, edited by K. J. Reutter et al., 333 pp., Springer, Heidelberg.
Robinson, R. A., S. Binnie, G. González, and J. Cortés (2011), Dating upper plate normal fault slip events in Late Pleistocene and Holocene sediments of northern Chile, in: *AGU Fall Meeting Abstracts*, *1*, 2011, p. 08.
Scheuber, E., and P. A. M. Andriessen (1990), The kinematic and geodynamic significance of the Atacama fault zone, northern Chile, *J. Struct. Geol.*, *12*(2), 243–257.
Scheuber, E., and K. J. Reutter (1992), Magmatic arc tectonics in the Central Andes between 21° and 25°S, *Tectonophysics*, *205*(1–3), 127–140.
Schlunegger, F., G. Zeilinger, A. Kounov, F. Kober, and B. Hüsser (2006), Scale of relief growth in the forearc of the Andes of Northern Chile (Arica latitude, 18°S), *Terra Nova*, *18*(3), 217–223.
Shirzaei, M., R. Bürgmann, O. Oncken, T. R. Walter, P. Victor, and O. Ewiak (2012), Response of forearc crustal faults to the megathrust earthquake cycle: InSAR evidence from Mejillones Peninsula, northern Chile, *Earth Planet. Sci. Lett.*, *333–334*, 157–164.
Sibson, R. H. (1989), Earthquake faulting as a structural process, *J. Struct. Geol.*, *11*(1–2), 1–14.
Slemmons, D. B. (1957), Geological effects of the Dixie Valley-Fairview Peak, Nevada, earthquakes of December 16, 1954, *Bull. Seismol. Soc. Am.*, *47*(4), 353–375.
Stirling, M., D. Rhoades, and K. Berryman (2002), Comparison of earthquake scaling relations derived from data of the Instrumental and Preinstrumental Era, *Bull. Seismol. Soc. Am.*, *92*(2), 812–830.
Strahler, A. N. (1957), Quantitative analysis of watershed geomorphology, *Civ. Eng.*, *101*, 1258–1262.
Thiele, R., and M. Pincheira (1987), Tectonica transpresiva y movimiento de desgarre en el segmento sur de la zona de Falla Atacama, Chile, *Rev. Geol. Chile*, *31*, 77–94.
Tichelaar, B. W., and L. J. Ruff (1991), Seismic coupling along the Chilean subduction zone, *J. Geophys. Res.*, *96*(B7), 11,997–12,022, doi:10.1029/91JB00200.
Vargas, G., L. Ortlieb, and J. Rutllant (2000), Aluviones históricos en Antofagasta y su relación con eventos El Niño/Oscilación del Sur, *Rev. Geol. Chile*, *27*, 157–176.
Vargas, G., J. Rutllant, and L. Ortlieb (2006), ENSO tropical-extratropical climate teleconnections and mechanisms for Holocene debris flows along the hyperarid coast of western South America (17°–24°S), *Earth Planet. Sci. Lett.*, *249*(3–4), 467–483.
Victor, P., B. D. Schurr, M. Sobiesiak, O. Ewiak, and O. Oncken (2012), The contribution of remotely triggered displacement events to the long-term strain accumulation along the Atacama Fault System, N-Chile, Abstract T22C-04 presented at 2012 Fall Meeting, AGU, San Francisco, Calif., 3–7 Dec.
Wallace, R. E. (1977), Profiles and ages of young fault scarps, north-central Nevada, *Geol. Soc. Am. Bull.*, *88*(9), 1267–1281.
Wallace, R. E. (1980), Degradation of the Hebgen Lake fault scarps of 1959, *Geology*, *8*(5), 225–229.
Wallace, R. E. (1984), *Faulting Related to the 1915 Earthquakes in Pleasant Valley, Nevada, U.S. Geol. Surv. Prof. Pap.*, vol. 1274-A, B, U.S. Gov. Print. Off., Wash.
Walsh, J. J., A. Nicol, and C. Childs (2002), An alternative model for the growth of faults, *J. Struct. Geol.*, *24*(11), 1669–1675.
Weissel, J. K., and M. A. Seidl (1997), Influence of rock strength properties on escarpment retreat across passive continental margins, *Geology*, *25*(7), 631–634.
Wells, D. L., and K. J. Coppersmith (1994), New empirical relationships among magnitude, rupture length, rupture width, rupture area, and surface displacement, *Bull. Seismol. Soc. Am.*, *84*(4), 974–1002.
Wesnousky, S. G. (2006), Predicting the endpoints of earthquake ruptures, *Nature*, *444*(7117), 358–360.
Whipple, K. X., and G. E. Tucker (1999), Dynamics of the stream-power river incision model: Implications for height limits of mountain ranges, landscape response timescales, and research needs, *J. Geophys. Res.*, *104*(B8), 17,661–17,674, doi:10.1029/1999JB900120.
Yanites, B. J., G. E. Tucker, K. J. Mueller, and Y.-G. Chen (2010), How rivers react to large earthquakes: Evidence from central Taiwan, *Geology*, *38*(7), 639–642.

Erratum

In the originally published version of this article, the supporting information summary file (tect20238-sup-0001-README.TXT) and supporting text file (tect20238-sup-0002-supplementary.docx) contained incorrect figure numbering for the supporting figures, as well as the incorrect publication year. These files have since been corrected and this version may be considered the authoritative version of record.